

NUMERICAL SIMULATION OF HUMAN BREATHING AND PARTICLE TRANSPORT
THROUGH A CT-BASED PULMONARY AIRWAY GEOMETRY

By

Richard R. Gruetzemacher, III

Abdollah Arabshahi
Research Professor,
Computational Engineering
(Chairperson/Principal Adviser)

Kidambi Sreenivas
Research Professor,
Computational Engineering
(Committee Member)

Ramesh Pankajakshan
Research Professor,
Computational Engineering
(Committee Member)

Roger W. Briley
Professor Emeritus,
Computational Engineering
(Committee Member)

NUMERICAL SIMULATION OF HUMAN BREATHING AND PARTICLE TRANSPORT
THROUGH A CT-BASED PULMONARY AIRWAY GEOMETRY

By

Richard Ross Gruetzemacher, III

A Thesis Submitted to the Faculty of the University of
Tennessee at Chattanooga in Partial Fulfillment
of the Requirements of the Degree of Master of
Science: Engineering

The University of Tennessee at Chattanooga
Chattanooga, Tennessee

December 2014

ABSTRACT

Chronic respiratory illness afflicts more than a billion people worldwide. In recent years computational fluid dynamics (CFD) has been established as a paramount tool for studying treatments of respiratory illnesses. This work investigates physiologically appropriate, lobar-specific boundary conditions for numerical simulation of steady and unsteady flow through a computed tomography (CT) based pulmonary airway geometry. Particle transport is modeled in steady and unsteady flow. Analysis is conducted on flow phenomena and particle transport in both steady and inspiratory flow.

DEDICATION

For those who suffer from respiratory illness:

*When you want wisdom and insight as badly as you want to breathe,
it is then you shall have it.*

– Socrates, 5th c. BCE

ACKNOWLEDGEMENTS

Foremost, a very sincere thanks goes to Dr. Abi Arabshahi, my adviser on this work, for the opportunity to tackle such a rewarding problem. His mentorship, guidance, and perpetual patience will forever be appreciated.

I would also like to thank Dr. Kidambi Sreenivas and Dr. Ramesh Pankajakshan for their interest and assistance over the course of the study. Their collective knowledge has been essential to my success. I also thank Dr. Roger Briley for his insight into the complex fluid physics in the airways.

I also wish to express thanks to Dr. Kent Hutson for his interest in this study, his medical expertise, and his assistance in obtaining an ideal set of CT images. I would like to thank Dr. Tamas Dolinay for contributing his ideas and Dr. Gregory Heath for his assistance in facilitating introductions with Dr. Hutson and Dr. Dolinay.

TABLE OF CONTENTS

ABSTRACT	iii
DEDICATION	iv
ACKNOWLEDGEMENTS	v
LIST OF TABLES	ix
LIST OF FIGURES	x
LIST OF ABBREVIATIONS	xii
LIST OF SYMBOLS	xiii
CHAPTER	
1. INTRODUCTION	1
1.1 Background	1
1.2 Statement of the Problem	2
1.3 Objectives of the Study	2
1.4 Scope	3
1.5 Significance of the Study	4
2. LITERATURE REVIEW	5
2.1 Experimental Work	5
2.2 Analytical Models	8

2.3 Early Computational Models	9
2.4 Recent Computational Models	10
2.5 Current Work	14
3. COMPUTATIONAL METHODS & VALIDATION.....	15
3.1 Flow Solver	15
3.1.1 Governing Equations.....	16
3.2 Validation	17
3.2.1 Ma <i>et al.</i>	18
3.2.2 Ramuzat & Riethmuller.....	22
3.2.3 Womersley	25
3.3 Boundary Conditions.....	30
3.3.1 Physiologically Appropriate Flow Rates.....	30
3.3.2 Lobar-Specific Boundary Conditions.....	30
3.4 Particle Models	32
4. CT-BASED AIRWAY GEOMETRY & MESH GENERATION	33
4.1 CT Imagery Acquisition	33
4.2 Geometry Generation.....	34
4.2.1 Imaging & Volume Rendering.....	34
4.2.2 Segmentation.....	35
4.2.3 Surface Reconstruction.....	35
4.3 Mesh Generation	37
4.3.1 Structured Surface Mesh	37
4.3.2 Hybrid Volume Mesh	39
4.3.3 Distal Airway Extensions	39
5. PULMONARY AIRFLOW MODELS	40
5.1 Steady Flow	40

5.2 Unsteady Flow.....	43
5.3 Particle Transport.....	54
6. CONCLUSIONS.....	59
7. FUTURE WORK	62
REFERENCES.....	65
VITA.....	71

LIST OF TABLES

5.1	Deposition fraction and final particle location data from steady particle transport models with and without the effects of hygroscopy, $\alpha = 4.72$	56
5.2	Deposition fraction and final particle location data from unsteady particle transport models with and without the effects of hygroscopy, $\alpha = 4.72$	56
5.3	Deposition fraction and final particle location data from steady particle transport models with and without the effects of hygroscopy, $\alpha = 6.68$	58
5.4	Deposition fraction and final particle location data from unsteady particle transport models with and without the effects of hygroscopy, $\alpha = 6.68$	58

LIST OF FIGURES

3.1	The idealized, alveolated airway geometry of the Ma <i>et al.</i> study used for validation shown with the results for CFD particle trajectories for the 7 particle release positions of the experiment.	19
3.2	A comparison of the experimental particle trajectories for particles 1-4 of Ma <i>et al.</i> with the CFD particle trajectories from <i>Tenasi</i>	21
3.3	A comparison of the CFD solution from <i>Tenasi</i> and the experimental results from Ramuzat and Riethmuller for steady flow at a Reynolds number of 1000 at the end of the parent tube.	23
3.4	A comparison of experimental results from Ramuzat and Riethmuller with the CFD solution from <i>Tenasi</i> for $Re = 1000$ and $\alpha = 16.1$	24
3.5	The idealized tube geometry used for the Womersley validation case.	26
3.6	A comparison of the CFD solution from <i>Tenasi</i> and exact solution for pulsating flow through a tube; 0° to 180°	27
3.7	A comparison of the CFD solution from <i>Tenasi</i> and exact solution for pulsating flow through a tube; 180° to 360°	28
3.8	A comparison of deviation between the CFD solution from <i>Tenasi</i> and the exact solution for pulsating flow through a tube in 98k and 492k node meshes; 0° to 180°	29
3.9	A comparison of deviation between the CFD solution from <i>Tenasi</i> and the exact solution for pulsating flow through a tube in 98k and 492k node meshes; 180° to 360°	29
4.1	A 9-generation surface reconstruction of the pulmonary airways from a set of standard resolution CT images after cleaning of erroneous surfaces.	36

4.2	A structured surface mesh and 625k node hybrid mesh generated from a 9-generation surface reconstruction of a set of standard resolution CT images.	38
5.1	Cross-sections from each lobar bronchus orthogonal to the axial flow. These cross sections are labeled by the lobar bronchi; RS (right superior), RM (right middle), RI (right inferior), LS (left superior), and LI (left inferior).	42
5.2	A numerical solution from <i>Tenasi</i> for complete breathing cycle from rest. This solution is for tidal breathing with 4.72 (phase angles are shown from 0° to 360° at 45° intervals).	45
5.3	A comparison of secondary flows in an unsteady solution at \bar{V}_{\max} (left) and $\alpha = 4.72$ with a steady solution for $Re = 875$ (right) in the left inferior lobar bronchus.	47
5.4	A comparison of secondary flows in an unsteady solution at \bar{V}_{\max} (left) and $\alpha = 6.68$ with a steady solution for $Re = 1750$ in the right superior bronchus.	47
5.5	A comparison of secondary flows into the left inferior bronchus at $\pi/6$, $\pi/3$, and $\pi/2$	49
5.6	A comparison of secondary flows into the right middle bronchus at $\pi/6$, $\pi/3$, and $\pi/2$	49
5.7	A comparison of secondary flows into the right superior bronchus at $\pi/6$, $\pi/3$, and $\pi/2$	50
5.8	A comparison of secondary flows into the left inferior bronchus at $\pi/6$, $\pi/3$, and $\pi/2$	52
5.9	A comparison of secondary flows into the right middle bronchus at $\pi/6$, $\pi/3$, and $\pi/2$	52
5.10	A comparison of secondary flows into the right superior bronchus at $\pi/6$, $\pi/3$, and $\pi/2$	53

LIST OF ABBREVIATIONS

CFD, computational fluid dynamics

CFL, Courant-Friedrichs-Lewy number

CT, computed tomography

DF, deposition fraction

ELCAP, Early Lung Center Action Program

HRCT, high-resolution computed tomography

IRB, Institutional Review Board

MDCT, multiple detector computed tomography

PIV, particle image velocimetry

PTV, particle tracking velocimetry

Re, Reynolds number

St, Stokes number

UTCOMC, University of Tennessee College of Medicine, Chattanooga

LIST OF SYMBOLS

α , Womersley number

A_{out} , outflow area

a_t , grid speed

β , artificial compressibility parameter

C_D , coefficient of drag

ϵ , solution deviation

D_p , particle diameter

\vec{F} , inviscid fluxes

\vec{F}_p , total force on particle

\vec{G} , viscous fluxes

J_n , Bessel function of the first kind and order n

μ , molecular viscosity

ν , kinematic viscosity

\hat{n} , unit normal vector

$\hat{n}_x, \hat{n}_y, \hat{n}_z$, unit normal vector components in x, y , and z directions

Ω , control volume

$\partial\Omega$, control volume surface

ω , angular velocity

ϕ , phase angle

P , pressure

P^* , complex conjugate of pressure

Q , conservative dependent variable vector

r , internal radius

R , radius

τ_{ij} , viscous stresses

T , period

t , time

u_p , velocity vector for particle

\vec{U}_r , velocity of particle relative to surrounding fluid

U_r , magnitude of relative velocity

u, v, w , fluid velocity components in x, y , and z directions

$\Delta\mathcal{V}_{\text{lobe}}$, change in lobar volume during inspiration

\bar{V}_{max} , maximum mean velocity

\vec{V}_{out} , outflow velocity vector

w^* , normalized axial velocity component

\hat{w} , estimator of the axial velocity mean

x_p , position vector for particle

x, y, z , Cartesian coordinate directions

CHAPTER 1

INTRODUCTION

The study of airflow in the lungs is of significant interest to researchers and medical professionals concerned with all varieties of respiratory illness. *In vitro* and *in vivo* techniques for studying this flow regime are limited; however, *in silico* models using computational fluid dynamics (CFD) offer unique insight into the complex fluid physics of pulmonary airflow. Numerical simulation is currently used for the study of pharmaceutical aerosol delivery and airborne contaminant transport. In the future, numerical simulation stands to play a critical role in patient-specific treatment of respiratory illness.

1.1. Background

Respiratory illness is the third leading cause of death in the United States, responsible for over 400,000 deaths annually. More than 1 in 10 Americans suffer from chronic lung conditions. Given the prevalence and ramifications of respiratory illness it is important to understand the mechanisms of pulmonary airflow and particle transport during respiration.

Over the past two decades great strides have been made regarding the fidelity of *in silico* models of pulmonary airflow and particle transport. Early modeling began on

simple, idealized bifurcations. Now, modeling is conducted on CT-based geometries, most of which are of a resolution exceeding that of the geometry used in this study. The use of CT-based geometries in numerical simulation of pulmonary airflow offers a means of viewing flow phenomena beyond the capabilities of experimentation. Currently, numerical simulation plays a significant role in the design of delivery devices of pharmaceutical aerosols. As model fidelity increases it promises to offer greater benefits to respiratory health.

1.2. Statement of the Problem

To date, the effects of inhalation transience on particle transport through a CT-based geometry have not been examined. The vast majority of studies of particle transport through patient-specific, CT-based airway geometries rely on the assumption that airflow through the airways can be assumed quasi-steady for modeling particle transport. Given interest from researchers regarding aerosol transport and potential clinical applications of airflow and particle transport modeling, higher-fidelity models should be examined.

1.3. Objectives of the Study

The primary objective of this study is to demonstrate a novel method for modeling airflow and particle transport through the pulmonary airways. A variety of ancillary objectives were identified to assist in achieving the primary objective and substantiating the results.

Three of these ancillary objectives concerned the validation of the numerical methods employed in the study. Each of these concerned modeling a flow regime characteristic of flow through the pulmonary airways. Another of the ancillary objectives was the geometry and mesh generation of the pulmonary airways from a set of CT images.

The final ancillary objective was the implementation of physiologically appropriate, lobar-specific boundary conditions for modeling steady flow through a CT-based geometry. Following this, the primary objective – implementation of these boundary conditions in unsteady flow – was completed. Particle transport models were then incorporated in both the steady and unsteady cases.

1.4. Scope

There are many limitations to this study. Significant limiting factors are the quality of the geometry constructed from CT images and simplifying assumptions regarding the modeling of the airway motion during breathing. Features to enhance the geometry, such as the inclusion of the upper airways and higher resolution rendering of the geometry from CT imagery, are beyond the scope of this study. Similarly, the effects of airway wall motion are beyond the scope of this study.

The variety of cases run is also limited. Only a single geometry is examined. The modeling of particles is conducted with limited sample sizes. Only two breathing rates are examined, both for breathing at rest, and only simple, symmetric inhalation waveforms are modeled.

1.5. Significance of the Study

This study demonstrates a novel framework for modeling human breathing and particle transport. This framework will enable future collaboration with researchers and medical professionals for conducting high-fidelity numerical simulations of breathing and particle transport. Particularly, this work provides the tools for studying the effects of various transient inhalation waveforms on airborne contaminant and pharmaceutical aerosol transport. The tools provided by this study stand to benefit public health, employees exposed to high levels of airborne contaminants in the workplace, and all other persons suffering from various forms of respiratory disease.

CHAPTER 2

LITERATURE REVIEW

2.1. Experimental Work

The groundwork for the study of airflow through the human pulmonary airways was laid by E.R. Weibel in 1963 [1]. Weibel recorded lung measurements of cadavers ranging in age from 8 to 64 years. Based on his data and observations he compiled an exhaustive text describing the morphology of the lung in which he proposed two models for studying the dichotomy of the airways. Weibel asserted that, for many purposes, the irregular dichotomy of the bronchial airways could be ignored. For such cases he set forth the *Model A*; an idealized, planar, symmetric network of bifurcations with each generation having uniform dimensions and being of equal distance from the origin. For cases in which the regular dichotomy of *Model A* was inadequate he set forth the *Model B*. This model described the irregular dichotomies typical of the physiological features observed in his study. The model was characterized by the irregular distributions of observed diameters in the observed generations.

Between 1967 and 1971, studies by Horsfield, Cumming, and colleagues [2-4] were conducted to expound upon the work of Weibel. The goal was to develop a more detailed framework that included a quantitative description of the irregular dichotomy in the pulmonary airways. Data was collected from measurements of a single lung cast.

This data was analyzed using a punch-card computer. Two quantitative descriptions were proposed detailing the nature of the branching patterns. A *Model 1* was developed assuming the mean asymmetry of each lobe as independent whereas a *Model 2* was developed assuming the mean asymmetry of each bronchopulmonary segment as independent. Notably, each of these models describes the geometry of an asymmetric network of bifurcations. An analysis of the transition zone of bifurcation between a parent tube and its two daughter tubes was also conducted. These models, like those of Weibel, have been heavily relied upon for numerical and experimental studies of airflow through the pulmonary airways.

Based on the models set forth by Weibel and Horsfield *et al.* experiments were conducted examining the characteristics of flow through these idealized bifurcating networks. Most notably Olson, while working with Horsfield, carried out extensive experimentation [5] on fluid flow through curved and elliptical tubes in bifurcating networks. Olson's experimentation and analysis lead him to conclude that, for the purposes of most study, airflow in the airways could be assumed quasi-steady and the motion of the airways could be ignored for normal breathing rates. These assumptions have been applied nearly ubiquitously since.

A rigorous examination [6] of specific features of bronchial bifurcations was presented by Hammersley and Olson in 1992. Their analysis was based on measured data from four lung casts and included measurements of additional anatomic features not considered by Horsfield *et al.* An alternative model for the bifurcation region was developed including a new model for the transition zone between parent and daughter

tubes with an emphasis on the ridge formed at the onset of the daughter tubes, the carinal ridge. Significant distinctions from the description given by Horsfield *et al.* are carinal ridge sharpness and the circular cross section of the proximal end of daughter branches adjacent to the carinal ridge.

In 1995, Heistracher and Hoffman [7] proposed a physiologically realistic bifurcation (PRB) defined by as many as 9 functions. Their model drew heavily from the data and simple model of Hammersley and Olson. Features of Weibel's models and the models of Horsfield *et al.* were also considered. The primary distinctions between the PRB and the model of Hammersley and Olson are the generality of the PRB and a detailed description of the carinal ridge geometry in the plane of bifurcation. It is of significance here to note that Hammersley and Olson stressed the complexity of the carinal ridge geometry and noted difficulties in measurement and description of the entire carinal region.

Since the early 2000s advances in experimental techniques allowed for notable improvements in data collection and the observation of flow phenomena. Fresconi *et al.* [8, 9] conducted a pair of experiments beginning with a simple, idealized bifurcation followed by an idealized, 3-generation model. These experiments employed particle image velocimetry (PIV) and particle tracking velocimetry (PTV). Theunissen and Riethmuller [10] also conducted an experiment using PIV and PTV on an idealized, 3-generation model including an alveolated bend.

Ma *et al.* [11] conducted an experimental examination of flow through an idealized, asymmetric, 3-generation model of alveolated airways. This study was

significant in that it included particles and compared experimental results with CFD models of the flow profiles and particle trajectories. The CFD results were found to be in acceptable agreement with the experimental results.

The unsteady nature of flow through the airways was examined by Tanaka *et al.* [12] in an experimental study using a 5-generation model based on the work of Horsfield *et al.* Flow was driven by two bellows pumps with resistors used at the distal branches to impose regional flow rates based on data from Horsfield *et al.* Ramuzat and Riethmuller [13] conducted an experimental study of unsteady, oscillating flow in a 3-generation geometry. This study employed separate pistons at the end of terminal branches to drive the flow and used PIV.

2.2. Analytical Models

Experimental observations by Pedley *et al.* [14-17] indicated that viscous energy dissipation downstream from bifurcations was always greater than that in Poiseuille flow. From this behavior a theory of the factors governing energy dissipation was developed which agreed with experimental results. Pedley *et al.* [18] extended Olson's work by further analyzing his experimental data, conducting further experiments, and extensively scrutinizing the morphological models proposed by Weibel and Horsfield *et al.* The culmination of this work was an analytical model for fluid flow through planar, asymmetric airway models, such as those described by Horsfield *et al.* This work allowed for the calculation of the sequential pressure drops in bifurcating airways.

An analytical model of greater significance to the current study comes from work related to the pulsatile nature of blood flow in arteries carried out by Womersley [19]. Womersley derived an exact solution for flow in a pipe subjected to a pulsating pressure gradient for hemodynamic modeling:

$$w = \frac{P^* R^2}{i\mu\alpha^2} \left\{ 1 - \frac{J_0(\alpha r i^{3/2})}{J_0(\alpha i^{3/2})} \right\} e^{i\omega t}$$

Womersley's work is of significance in the study of oscillating, pulmonary airflow as a complete oscillatory flow can be treated as a case of pulsatile flow subject to a simple oscillatory wave. Of particular significance to this study is the dimensionless parameter α , the Womersley number, which is the ratio of the transient inertial force to the viscous force. The Womersley number, together with the Reynolds number, governs the dynamic similarity of pulsatile flows and is a critical parameter in experiments and simulations.

$$\alpha = R \sqrt{\omega/\nu} = \sqrt{2\pi \text{ReSr}}$$

2.3. Early Computational Models

Numerical simulation of airflow and particle deposition in the lungs has been ongoing for more than 20 years. The modeling of a simple bifurcation using CFD was first documented in 1990 [20, 21]. Over the remainder of the decade work on the problem continued and models grew in complexity. During this period models were created with more rigorous consideration of anatomical features [22] although they

remained planar. Particular attention was given to the transition region of bifurcations and the carinal ridge. Over the past decade, complex, non-planar, anatomical models have been created. van Ertbruggen *et al.* [23] approximated azimuth angles from bronchoscopic images to create a non-planar, asymmetric model adapted from the second model proposed by Horsfield *et al.* The general orientation of the resulting non-planar, asymmetric geometry was verified with CT and x-ray images. Boundary conditions were enforced at distal boundaries to induce regional flow rates proportional to lobar volume using data from Horsfield *et al.*

The generation of a surface mesh from CT images was first demonstrated in 1996 [24]. It was not until 2003, however, that the use of CFD to model airflow in a CT-based model was demonstrated [25]. The realistic model used in this study was an idealized, symmetric, non-planar geometry that had been generated in a previous study [26]. This model and the model of van Ertbruggen *et al.* addressed the implicit planarity of the models set forth by Weibel and Horsfield *et al.*

2.4. Recent Computational Models

The use of numerical simulation for the study of pulmonary airflow is multidisciplinary in nature and the direction of current work toward improvement over previous models is spread among a number of different directions.

Idealized models used in current studies are both non-planar and asymmetric although the use of CT imagery for geometry generation has become common [27-29].

The quality of airway models reconstructed from CT imagery has become an independent topic of research [30-32].

Some studies are being conducted including high-resolution reconstructions [33] of the most intricate features of the upper airways (i.e. the nasal cavity and its constituents). Such considerations including nasal inhalation may be significant in modeling the inhalation of airborne particles.

An alternate direction of progress can be found in studies employing novel techniques for approximating flow through large numbers of terminal airways. A study from 2008 [34] simply uses existing data mapping 17 generations of bifurcations to generate an idealized geometry. More interesting approaches attempt to resolve flow features for terminal airways numbering between 2^{12} and 2^{23} . One example of these approaches [35] couples 1D approximations of distal generations to the CFD resolved 3D generations resulting from CT-based surface reconstruction. Such techniques are required because resolving flow features for even 2^{10} terminal airways with any acceptable fidelity is intractable for those lacking significant computational resources. An alternative to the 1D modeling of terminal airways is a coupling method derived from multiscale stochastic coupling [36] employed in implementations of the Monte-Carlo method. Implementation requires the resolution of several airways to a designated terminal generation. The solutions from these airways are then stochastically enforced on all remaining terminal boundaries.

With the introduction of CT-based geometries into the modeling of pulmonary airflow the task of geometry generation became a requirement. Furthermore,

geometry generation is a non-trivial task. Much work has been done over the past decade toward increasing the resolution of surface reconstructions from CT imagery and these efforts continue.

Studies of mesh independence have been conducted for differing mesh types and resolutions [37-39]. These studies were conducted on idealized, anatomical models. Conclusions indicate that structured meshes are significantly more efficient and offer improved resolution of secondary flow features.

Typical boundary conditions for outflow boundaries prescribe mass flow rates proportional to lobar volume from the data of Horsfield *et al* [23, 25, 40]. Walters *et al.* [28] uses a stochastic coupling approach randomly mapping pressures at resolved interior locations to outflow boundaries of the same generation while applying a uniform velocity at the inlet. DeBacker *et al.* [41] used iterative methods to determine outflow pressures matching flow rates proportional to lobar volume based on the data of Horsfield *et al.*

Studies specifically addressing the physiological representation of airways were notably established by the proposed physiologically realistic bifurcation [7]. The collaborative work of Heistracher and Hoffman continued for nearly ten years though the focus drifted from the physiology of airway bifurcations toward the modeling of particle motion and its applications [42].

The collaborative work of researchers in North Carolina, namely Zhang and Kleinstreuer, over more than a decade constitutes the majority of study concerning unsteady flow and waveform driven breathing cycles. Initially addressing the problem

of cyclic flow in 2002 [43], they have continued to examine particle motion in reciprocating flow regimes [44]. Their work has significantly progressed and they continue to make steady progress increasing the general understanding of fluid behavior within the airways.

Generalizations drawn from observations of the effects of inhalation transience and the conclusions of initial studies by Zhang and Kleinstreuer [45, 46] call into question the validity of the quasi-steady assumption for studying pulmonary airflow and particle transport in CFD models. Substantial differences are observed between steady state particle flow and deposition and the particle flow and deposition resulting from enforcement of transient inhalation waveforms at boundaries. Zhang and Kleinstreuer have shown that enforcing the average of mean and maximum values of the peak velocity profile results in deposition fraction (DF) values that are in line with those of cyclic, unsteady flow. Further studies [47-49] produce results in qualitative agreement with the early studies.

Presently, studies are being conducted in China [50] modeling unsteady, cyclic, breathing driven by the fluid-structure interaction approximating the cyclic change of the pleural pressure gradient. At present they are limited to idealized extra-thoracic models. Limitations of this work include the lack of a CT-based geometry and the limited scope of motion driven bifurcating flow.

2.5. Current Work

Over the past year several studies were identified which were closely related to the work being conducted. A study from Mead-Hunter *et al.* [51] found the effects of moving walls on respiratory aerosol deposition fractions to be significant. Huang *et al.* [50] modeled unsteady, cyclic breathing using a fluid-structure interaction to emulate the changes in lung volume occurring during breathing (this study was limited to the trachea). A study from Johari *et al.* [52] examined the effects of simplifying assumptions to CT-based geometries concluding that such assumptions produced significant deviations in regions of high flow and marked cross-sectional shape transition.

Early last year a study [53] was identified that demonstrated methods for modeling breathing similar to objectives of this study. Feldman and Wagner used time-varying pressure at the proximal boundary to drive oscillating flow through three increasingly complex geometries. The initial geometry was a simple tube used for validation with the Womersley solution. The following case was a simple, idealized bifurcation. The final case was a 3-generation, idealized, CT-based geometry. This study was primarily concerned with modeling of high frequency oscillatory ventilation (HFOV) for which a proximal, time-varying pressure would be appropriate.

Late last year a study from Yin *et al.* [54] demonstrated novel methods for modeling regional, patient-specific ventilation rates using multiscale techniques and volume filling algorithms. This study used multiple detector computed tomography (MDCT) to allow inclusion of patient-specific airway motion. The study documents the patient-specific techniques employed and notes limitations of these techniques.

CHAPTER 3

COMPUTATIONAL METHODS & VALIDATION

This chapter describes the governing equations of interest, the numerical methods used for their solution, and the validation of these methods. The results of three validation cases are presented and boundary conditions for the CT-based geometry are discussed.

3.1. Flow Solver

Tenasi [55], a flow solver developed in-house at the SimCenter, was used in this study to generate numerical solutions for the Navier-Stokes equations. *Tenasi* uses a finite volume, implicit scheme with high-resolution fluxes. *Tenasi* was used to obtain both steady state (steady) solutions and time-accurate (unsteady) solutions. Solutions from *Tenasi* have been validated with experimental data and exact solutions for a wide variety of flow regimes [56]. Previously, *Tenasi* had not been validated for oscillating or bifurcating internal flows.

For steady solutions, local-time-stepping was used to accelerate convergence. Using this technique the appropriate time step was determined for each cell based on the Courant-Friedrichs-Lewy (CFL) number. CFL numbers of 50-250 were used.

For unsteady solutions a Newton iteration procedure was used, with a large number of iterations per time step, for time accuracy. Dual-time-stepping was used to aid stability during these Newton iterations. A very conservative CFL number, 0.025, was required for the stability of unsteady solutions.

The time step was dependent on the period and computed for each Womersley number. For a period of $T = 8\text{s}$, where $\alpha = 4.72$, the time step was set to $\Delta t \cong 0.001\text{s}$ and for a period of $T = 4\text{s}$, where $\alpha = 6.68$, the time step was set to $\Delta t \cong 0.000502008\text{s}$.

3.1.1. Governing Equations

Due to the relatively low Mach numbers characteristic of flow through the pulmonary airways the effects of compressibility were assumed negligible. This is consistent with all previous CFD cases concerning bifurcating internal flows cited in this study.

The unsteady three-dimensional incompressible Reynolds-averaged Navier-Stokes equations are appropriate for this study. These equations are presented here in conservative form and in Cartesian coordinates. The non-dimensional equations can be written in integral form as

$$\frac{\partial}{\partial t} \int_{\Omega} Q dV + \int_{\partial\Omega} \vec{F} \cdot \hat{n} dA = \frac{1}{Re} \int_{\partial\Omega} \vec{G} \cdot \hat{n} dA$$

Here, \hat{n} is the unit normal pointing outward from the control volume Ω . The vectors for the dependent variables, inviscid fluxes, and viscous fluxes are given as

$$Q = \begin{bmatrix} P \\ u \\ v \\ w \end{bmatrix}$$

$$\vec{F} \cdot \hat{n} = \begin{bmatrix} \beta(\Theta - a_t) \\ u\Theta - \hat{n}_x P \\ v\Theta - \hat{n}_y P \\ w\Theta - \hat{n}_z P \end{bmatrix}$$

$$\vec{G} \cdot \hat{n} = \begin{bmatrix} 0 \\ \hat{n}_x \tau_{xx} + \hat{n}_y \tau_{xy} + \hat{n}_z \tau_{xz} \\ \hat{n}_x \tau_{yx} + \hat{n}_y \tau_{yy} + \hat{n}_z \tau_{yz} \\ \hat{n}_x \tau_{zx} + \hat{n}_y \tau_{zy} + \hat{n}_z \tau_{zz} \end{bmatrix}$$

The velocity normal to the face of a control volume is defined as $\Theta = \hat{n}_x u + \hat{n}_y v + \hat{n}_z w + a_t$.

3.2. Validation

Despite the extensive validation of *Tenasi* for a wide variety of flow regimes three validation cases were completed, each representative of a unique case, for flow approximating the physiological flow conditions in the airways. These steps were taken to bolster the confidence in solutions on CT-based human airway geometries. This validation also served as a means of becoming familiar with the fluid physics of the flow regime and the effects of varying boundary conditions and numerical methods on such flow.

Of the three validation cases, one concerned experimental data for particle transport during steady flow through an idealized, asymmetric, alveolated airway. The

remaining two cases involved unsteady flow. One of these unsteady cases concerned experimental data for piston-driven oscillating flow through an idealized, symmetric, 3-generation geometry. The other unsteady case models Womersley's exact solution for pulsating flow through a simple tube.

3.2.1. Ma *et al.*

The first of the selected validation cases comes from the 2009 experimental study by Ma *et al* [11]. This experiment examined velocity profiles and particle transport through an idealized, asymmetric, alveolated airway geometry during steady flow conditions. This case was selected for validation because it contained experimental data for particle transport in a bifurcating, internal flow. The experimental results reported were accompanied by results from CFD models as well.

The geometry used in this experiment was developed to approximate the alveolated regions of the distal pulmonary airways. This asymmetric geometry was comprised of five airways in 3-generations with a uniform diameter of 20mm (45mm for the alveolar rings). The geometry can be seen in Figure 3.1. Flow conditions were based on data from the Weibel model to be representative of flow through the 20th to 22nd generations. Consequently, a Reynolds number of 0.13, corresponding to a flow rate of 2.04 ml/s through the parent tube, was used for the experiment. PIV and PTV were used to capture velocity profiles and particle trajectories, respectively.

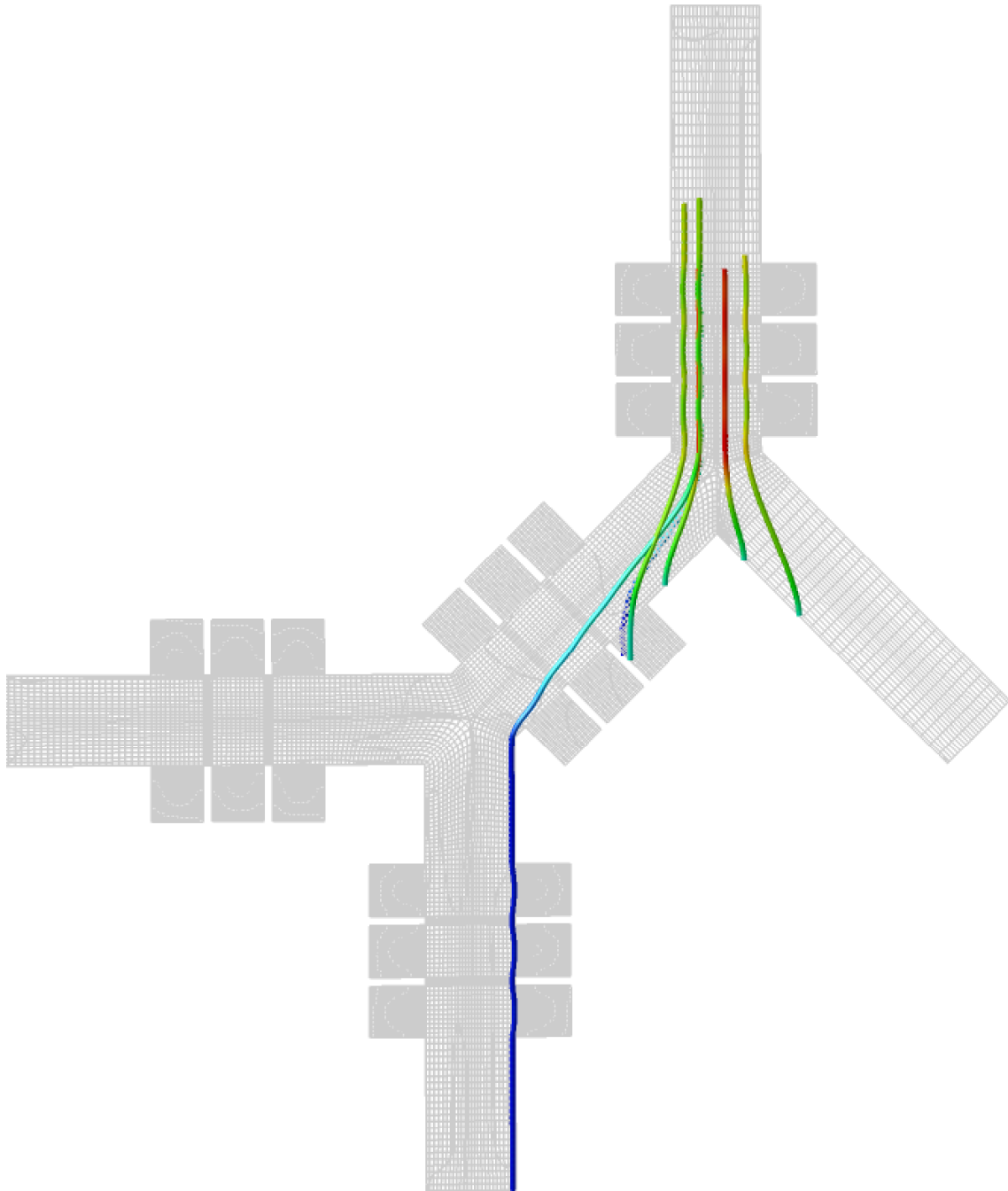


Figure 3.1

The idealized, alveolated airway geometry of the Ma *et al.* study used for validation shown with the results for CFD particle trajectories for the 7 particle release positions of the experiment.

The working fluid used in the experiment was silicone oil with a density of 970 kg/m³ and a dynamic viscosity of 1.0 Pa•s. 0.5mm and 1.2mm spherical iron beads were used to mimic aerosol *in vivo*. These spherical iron beads had a density of 7800 kg/m³ and were released from a variety of positions in the cross-section of the parent tube.

The properties specified for silicone oil and spherical iron beads were used in the validation case run on *Tenasi*. The three terminal airways in the experiment were equipped with flow meters and, from left to right, exhibited split flow ratios of 0.252, 0.244, and 0.504. For the validation case these ratios were replicated for each of the terminal airways while maintaining a total flow rate of 2.04 ml/s.

The validation case employed boundary conditions of fixed pressures and floating velocities at inflow and outflow boundaries. The pressure at the inflow boundary was fixed to atmospheric pressure. The pressures at the outflow boundaries were determined iteratively to match the desired flow rates for each boundary.

Experimental results were manually digitized to minimize error. Experimental axial velocity profiles from nine cross sections were compared to the steady solution from *Tenasi*. The numerical results were determined to be in good agreement with the experimental results. The maximum deviation between the solutions was less than 6%. The CFD results reported by Ma *et al.* exhibited a maximum deviation of ~5%.

A comparison of the particle trajectories for particles 1 through 4 can be seen in Figure 3.2. The results from *Tenasi* were deemed acceptable. Furthermore, no discernable difference in the quality was observed between the CFD particle trajectories reported by Ma *et al.* and the results from *Tenasi*.

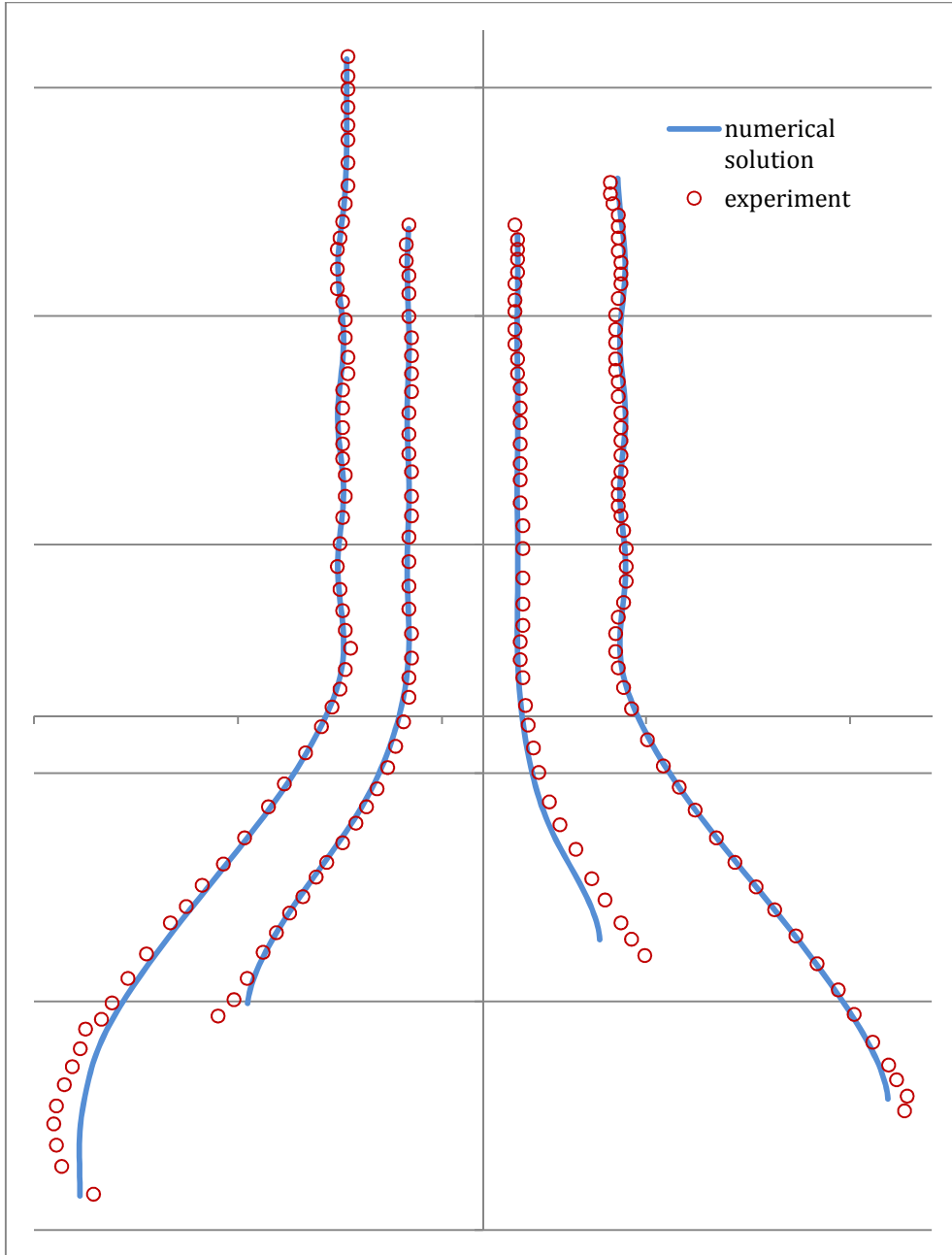


Figure 3.2

A comparison of the experimental particle trajectories for particles 1-4 of Ma *et al.* with the CFD particle trajectories from *Tenasi*.

3.2.2. Ramuzat & Riethmuller

The second of the selected validation cases comes from a 2002 experimental study by Ramuzat and Riethmuller [13]. This experiment examined piston-driven oscillating flow through an idealized, symmetric geometry. This geometry was comprised of 3-generations. The diameter of the parent tube was 2.0 cm with the diameter of each successive generation being scaled by a factor of 0.8. PIV techniques were employed in the experiment to measure velocity profiles.

The working fluid in the experiment was water. Four cases were modeled for validation. These cases included a baseline case of steady flow at a Reynolds number of 1000 and cases for oscillating flow at Womersley numbers of 3.6, 8.1, and 16.1 with Reynolds numbers peaking at 1000. Numerical solutions were obtained with *Tenasi* for each of these four cases.

For the baseline case of steady flow only a single velocity profile was reported, taken from a cross section at the distal end of the parent tube. This velocity profile was compared with the velocity profile from the *Tenasi* solution as seen in Figure 3.3. The experimental velocity profile is slightly shifted while the *Tenasi* solution is symmetric. The experimental velocity profile and the solution from *Tenasi* also deviate slightly in form, with the experimental velocity profile not being formed as fully as expected for laminar flow through a straight parent tube in a symmetric airway geometry. It is important to note, that, there is some uncertainty regarding the regions of bifurcation in the computational geometry due to a lack of data available regarding these regions in the experimental geometry.

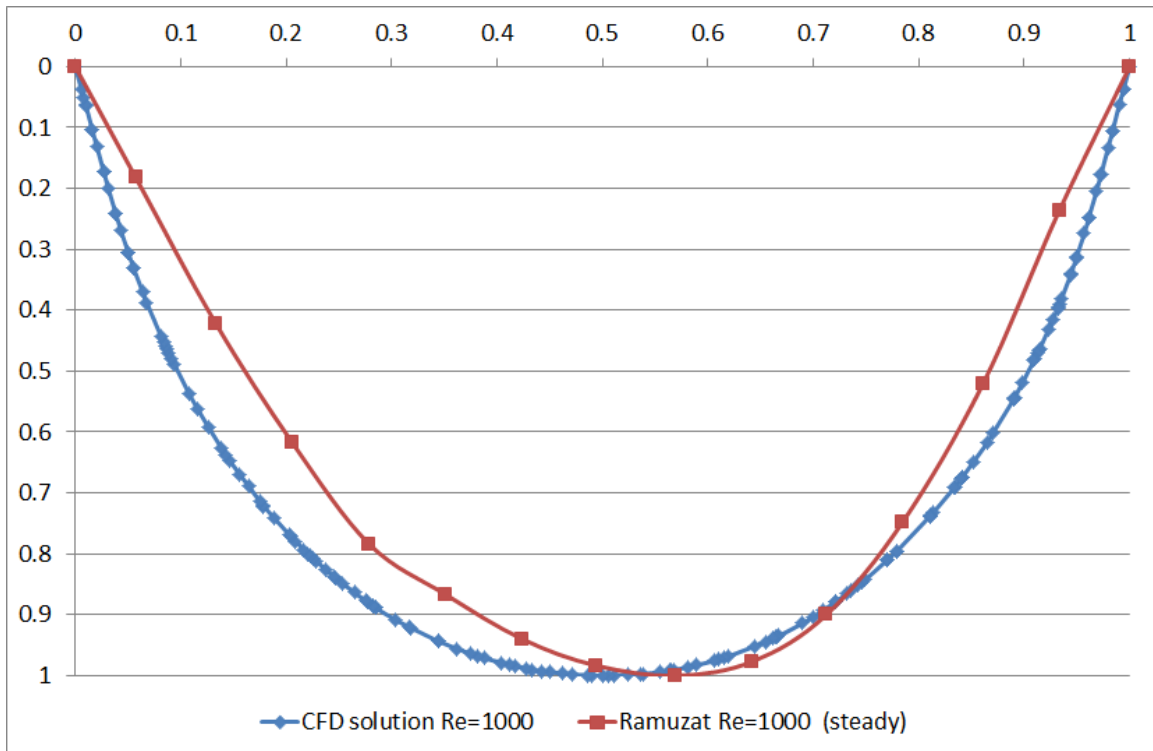


Figure 3.3

A comparison of the CFD solution from *Tenasi* and the experimental results from Ramuzat and Riethmuller for steady flow at a Reynolds number of 1000 at the end of the parent tube.

The remaining three solutions were for unsteady flow. A comparison of experimental results and the numerical solution for a Reynolds number of 1000 and $\alpha = 16.1$ is shown in Figure 3.4. The results are shown at phase angle increments of 45° over the course of an oscillation cycle. The numerical results deviate significantly from the experimental results and are not as desired. However, the waveforms for each phase angle, with the exception of $\phi = 90^\circ$, are all of the same form.

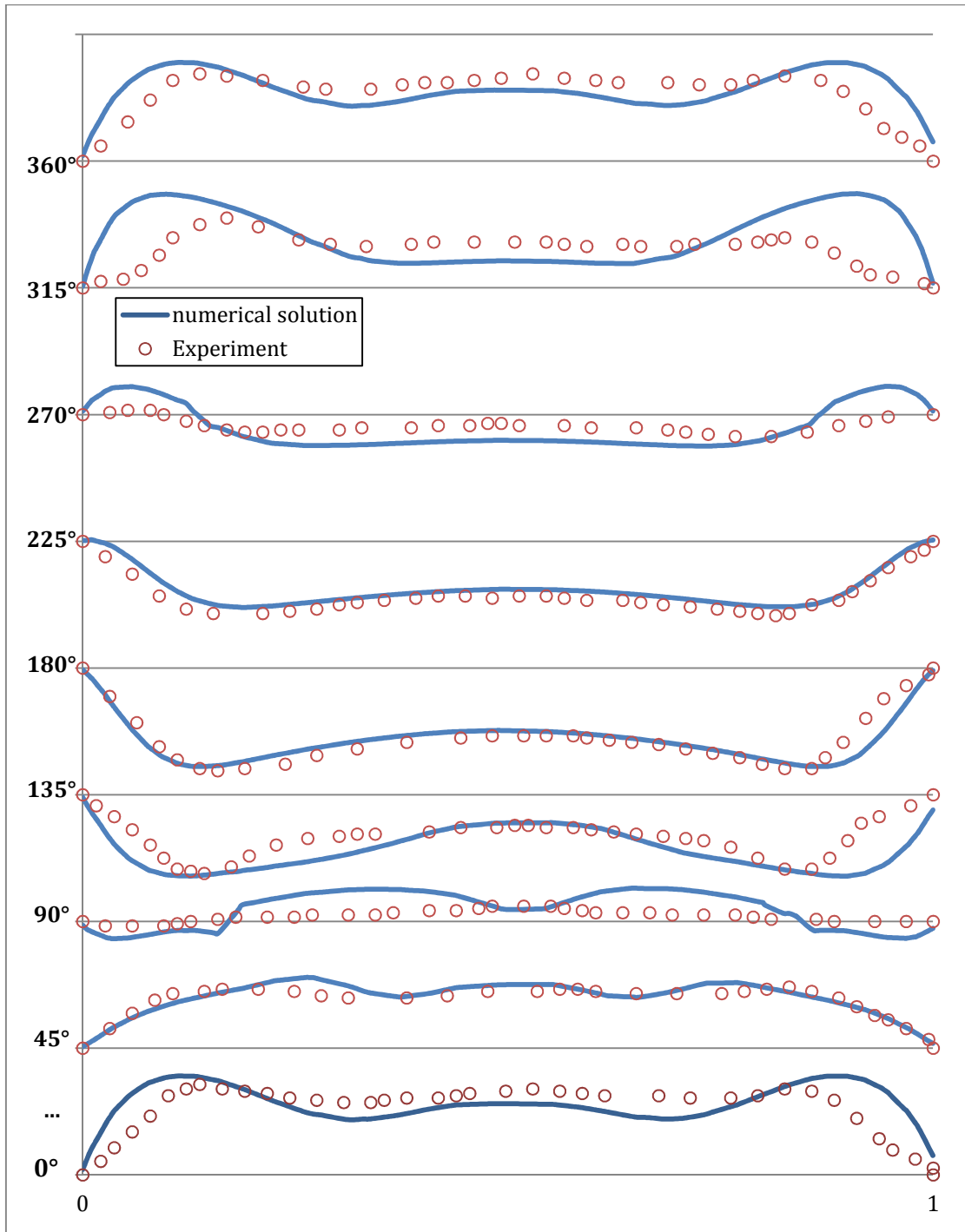


Figure 3.4

A comparison of experimental results from Ramuzat and Riethmuller with the numerical solution from *Tenasi* for $Re = 1000$ and $\alpha = 16.1$.

The significant deviation is potentially a result of the boundary conditions used for modeling the experiment. Oscillating pressures were used at boundaries, as in the Womersley validation case. This oscillating pressure gradient was, however, applied at four distal boundaries rather than a single proximal boundary, as in the Womersley validation. The fluid flow in the experiment was driven by pistons at the distal boundaries. The use of an oscillating pressure gradient at distal boundaries in the validation case may not be an appropriate approximation of the physical conditions present in the experiment. Moreover, the poor quality of the experimental results for the baseline case may be indicative of quality issues in unsteady experimental results. The effects of the uncertainty about the regions of bifurcation could also play a factor.

3.2.3. Womersley

The third of the selected validation cases sought to replicate the Womersley solution [19] for pulsating flow in a tube. This validation case was also used to assess mesh convergence in oscillating flow. Figure 3.6 depicts the idealized tube geometry. Numerical solutions were extracted at a length to diameter ratio of 15.

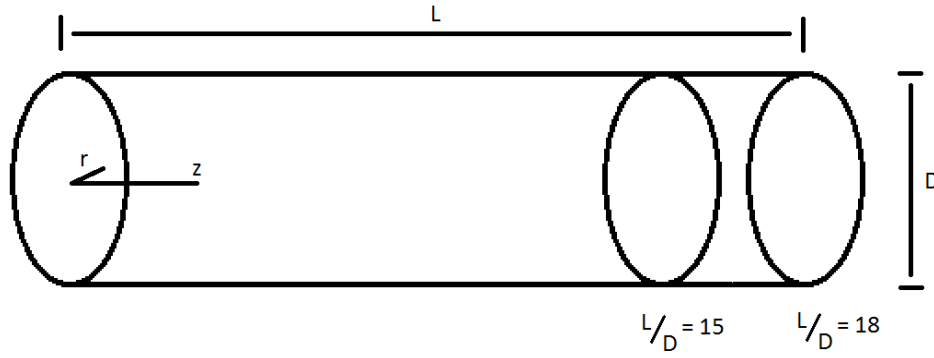


Figure 3.5

The idealized tube geometry used for the Womersley validation case.

A numerical solution for pulsating flow through a tube at a Womersley number of $\alpha = 4.72$ was obtained with *Tenasi*. The results are depicted for phase angles of 0° to 180° in Figure 3.5 and phase angles 180° to 360° in Figure 3.6. Three hybrid meshes were used to test for mesh convergence. These included a 20k node mesh, a 98k node mesh, and a 492k node mesh. Defining w^* by

$$w^*(r, \phi) = \frac{w(r, \phi)}{\hat{w}_{\text{exact}}}$$

we can define the deviation of the numerical solution from the exact solution as

$$\epsilon(\phi) = \sum_{i=1}^{N_R} |w_{\text{CFD}}^*(r_i, \phi) - w_{\text{exact}}^*(r_i, \phi)| \Delta r_i$$

The deviation between numerical solutions and the exact solution is shown in Figure 3.7 and Figure 3.8. Deviation is shown for the 98k node mesh and the 492k node mesh – the deviation was not computed for the 20k node mesh as the appropriate point along the length of the tube was not identified for extracting the solution.

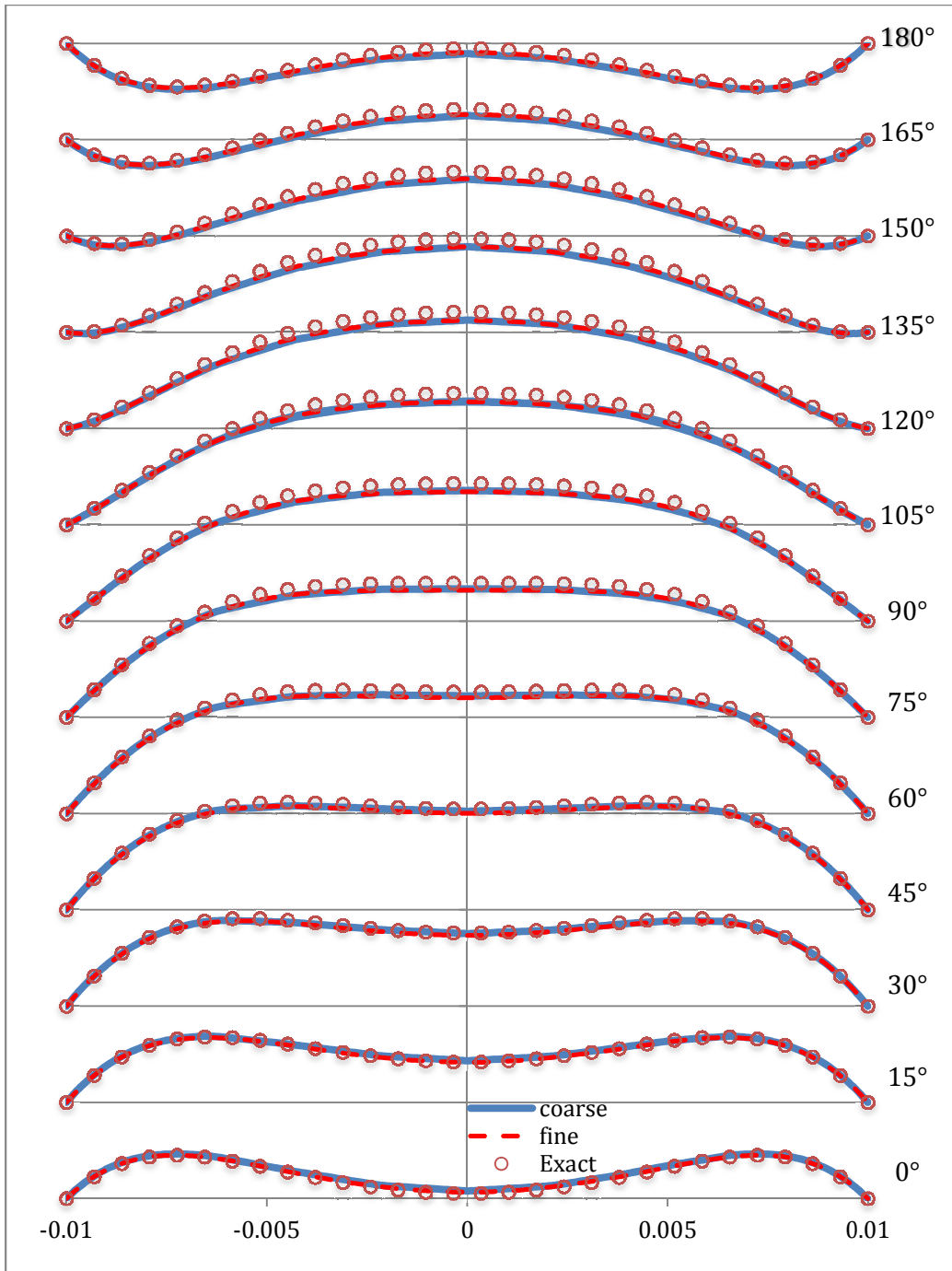


Figure 3.6

A comparison of the numerical solution from *Tenasi* and exact solution for pulsating flow through a tube; 0° to 180°.

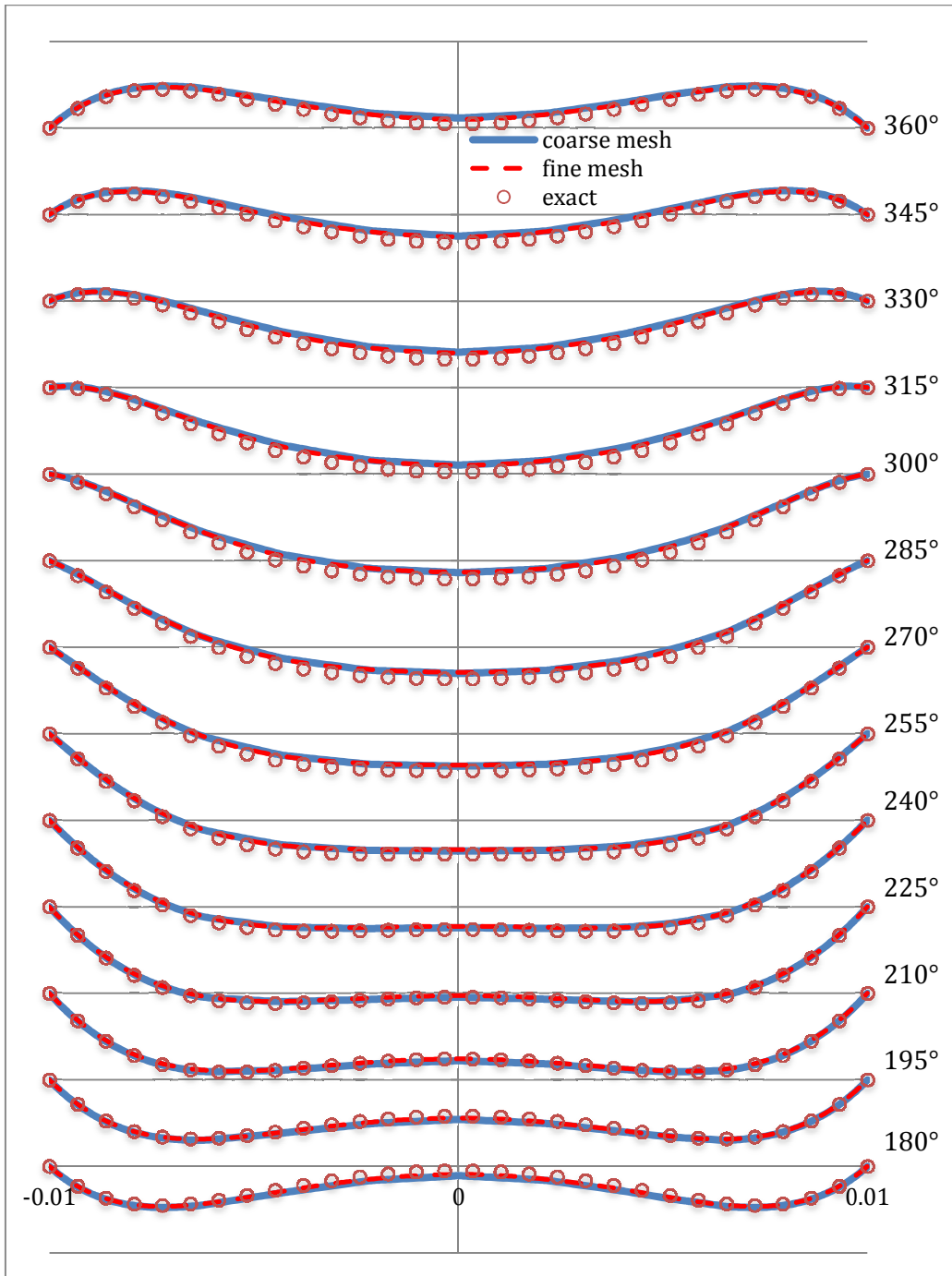


Figure 3.7

A comparison of the numerical solution from *Tenasi* and exact solution for pulsating flow through a tube; 180° to 360°.

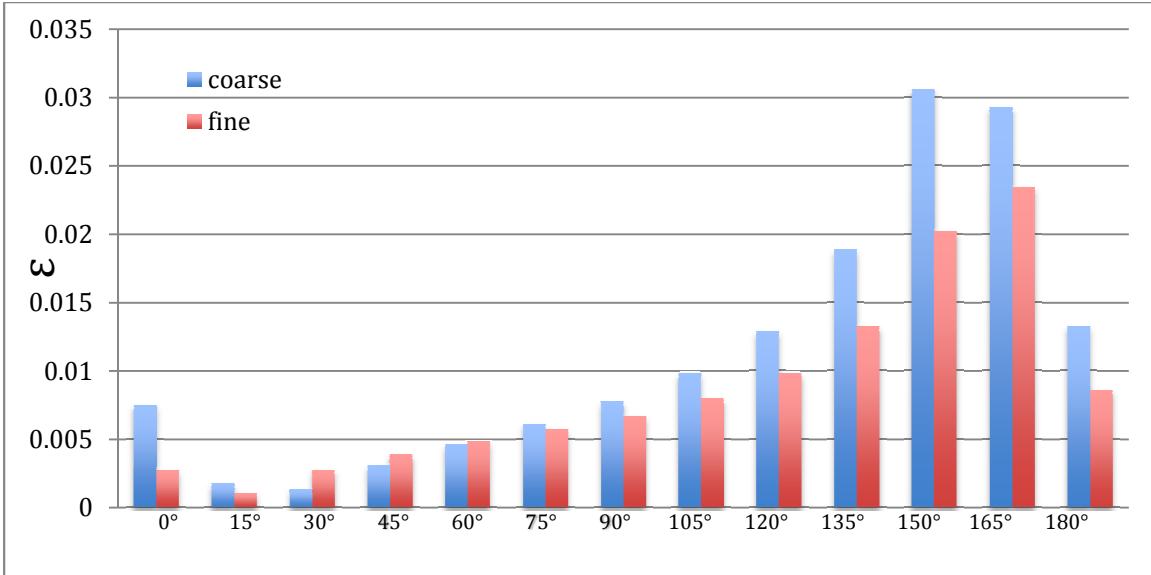


Figure 3.8

A comparison of deviation between the numerical solution from *Tenasi* and the exact solution for pulsating flow through a tube in 98k and 492k node meshes; 0° to 180°.

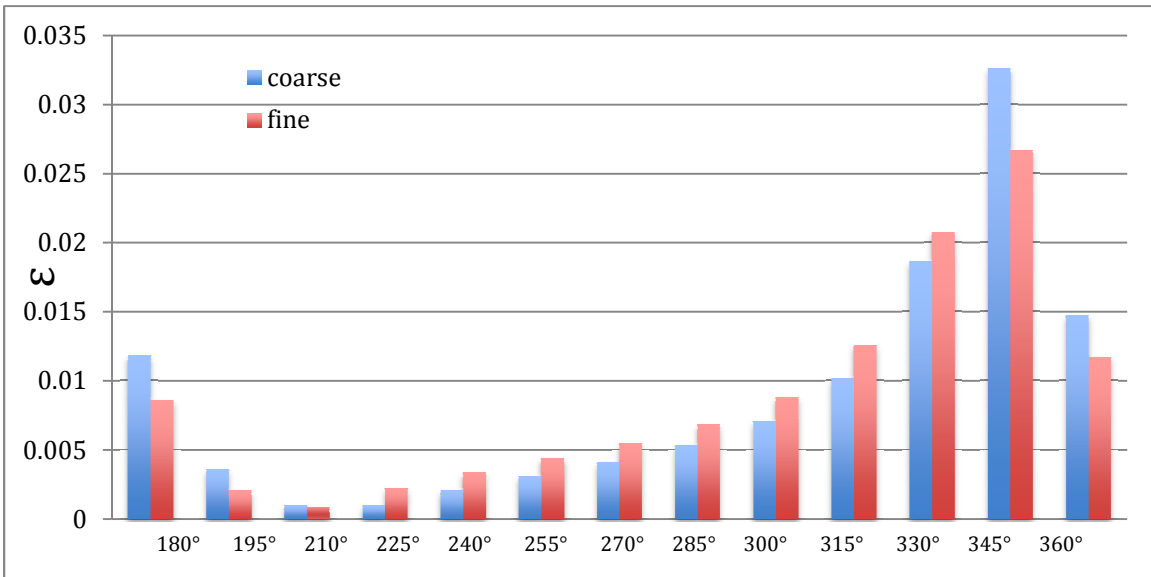


Figure 3.9

A comparison of deviation between the numerical solution from *Tenasi* and the exact solution for pulsating flow through a tube in 98k and 492k node meshes; 180° to 360°.

3.3. Boundary Conditions

3.3.1. Physiologically Appropriate Flow Rates

Regional ventilation rates are a significant consideration when modeling airflow through patient-specific, CT-based geometries. Airflow in the lungs is driven by the volume change in the lungs, and this volume change is regional. Flow rates through each bronchi are consequent of distal volume changes. Parenchymal volume distal to each lobar bronchus and each tertiary bronchus can be determined with an acceptable degree of precision to enforce patient-specific, regional flow rates through the airways. Consideration of these factors precludes the use of a single proximal boundary condition to drive flow when modeling the natural cycle of human inspiration and expiration.

For the purposes of this study patient-specific flow rates were not considered. A rather simple method was employed for approximating the appropriate regional flow rates. This method, however, allows for the demonstration of techniques that can be applied with more thorough methods for determining appropriate physiological conditions. The flow rates were computed based on lobar volumetric data of Horsfield *et al.* [4]. Enforcing such boundary conditions for steady flow has precedent, however, there is no precedent for enforcing such boundary conditions in unsteady, cyclic flow.

3.3.2. Lobar-Specific Boundary Conditions

The lobar-specific boundary conditions are based on an approximate *a priori* known value for the change in lobar volume, ΔV_{lobe} . This value is monitored in each

lobe to ensure that the actual boundary conditions applied effectively induce this desired change.

Pure Dirichlet boundary conditions are used to apply a uniform velocity across distal lobar boundaries. At these boundaries the pressure is left to float. Alternately, at the proximal boundary a pure Dirichlet boundary condition is used to keep pressure static at standard atmospheric pressure. In this case velocities are left to float.

To obtain the appropriate velocities to enforce at lobar boundaries (in this case, for both steady and unsteady cases) an expression was written for $\Delta\mathcal{V}_{\text{lobe}}$ as a function of the maximum mean velocity, \bar{V}_{max} ,

$$\Delta\mathcal{V}_{\text{lobe}} = \bar{V}_{\text{max}}A_{\text{out}}\frac{T}{2\pi}\int_0^\pi \sin\phi d\phi$$

$$\Delta\mathcal{V}_{\text{lobe}} = \bar{V}_{\text{max}}A_{\text{out}}\frac{2}{\omega}$$

$$\bar{V}_{\text{max}} = \frac{\omega\Delta\mathcal{V}_{\text{lobe}}}{2A_{\text{out}}}$$

For steady cases the appropriate lobar \bar{V}_{max} is simply multiplied by the unit normal of each distal boundary. Similarly, the appropriate lobar-specific boundary conditions are applied for unsteady flow in

$$\vec{V}_{\text{out}} = \bar{V}_{\text{max}}\hat{n}\sin(\omega t)$$

3.4. Particle Models

Numerical solutions for particle trajectories are computed by solving [57] the following ordinary differential equations for position and velocity:

$$\frac{d}{dt} x_p = u_p$$
$$\frac{d}{dt} u_p = \frac{1}{m} \vec{F}_p + \vec{g}_p$$

where

$$\vec{F}_p = \vec{F}_{Drag} + \vec{F}_{Magnus} + \vec{F}_{Saffman} + \vec{F}_{AddedMass}$$

Drag is modeled by a drag equation:

$$\vec{F}_{Drag} = \frac{1}{8} C_D \rho \pi D_p^2 U_r \vec{U}_r$$

Here,

$$C_D = \frac{24}{Re_p} \left[1 + \frac{1}{6} Re_p^{2/3} \right]$$

In this study, only the drag force is considered.

CHAPTER 4

CT-BASED AIRWAY GEOMETRY & MESH GENERATION

This chapter describes the steps taken to use a CT-based geometry in this study. Initially steps were taken to acquire a set of CT images suitable for the study. Next, the CT images acquired were processed and a surface reconstruction was created. Finally, a mesh was generated for the resulting surface reconstruction.

4.1. CT Imagery Acquisition

Two sets of CT imagery were selected for surface reconstruction. One of these was standard resolution and the other high-resolution. The surface reconstruction from the standard resolution CT images was selected for mesh generation.

A variety of sets of CT images can be found on the Web. Cornell University maintains the ELCAP Public Lung Image Database [58]. This database contains 50 low-dose whole-lung sets of CT images. All of the CT imagery contained in this database is standard resolution, i.e. transverse slices of 256 x 256 voxels at 1.25 mm increments.

High-resolution computed tomography (HRCT) images were not found on the Web. The University of Tennessee College of Medicine, Chattanooga (UTCOMC) was contacted for assistance in acquiring the HRCT imagery desired for the study. After making contact with UTCOMC faculty, plans were made to obtain a set of HRCT images

of a healthy patient's chest. The use of patient data for research purposes requires approval from an institution's Institutional Review Board (IRB). In this case approval was required from both the UTC IRB and the UTCOMC IRB. A single research proposal was composed and submitted with the appropriate applications as required for each institution. Approval was granted from the IRB at each institution for the acquisition of de-identified HRCT thoracic imagery. Imagery from an ideal candidate was selected from patients at Erlanger Medical Center, de-identified, and provided for use in this study.

4.2. Geometry Generation

The generation of a geometry from CT imagery has two primary requirements: point cloud generation and surface reconstruction. Many different techniques can be used independently or combined when generating a point cloud from CT imagery. Two techniques were used in combination and will be discussed.

4.2.1. Imaging & Volume Rendering

An open source medical imaging software package was used for volume rendering prior to segmentation and point cloud generation. This package, Slicer3D, is licensed for non-commercial use only. The volume rendering performed by Slicer3D was effectively adept image filtering. Slicer3D offered preset volume rendering options for different morphological features of the body. The image filtering parameters for rendering vasculature was used.

4.2.2. Segmentation

Slicer3D offered several segmentation algorithms for potential use on the filtered images from the volume rendering. A level-set segmentation algorithm was selected and used. This algorithm required at least one seed point, and a seed was positioned at the carinal ridge at the bifurcation of the trachea.

The segmented volume resulting from the level-set segmentation had to next be exported as a point cloud. This required the generation of a surface model in Slicer3D. The segmented volume was selected, a surface model was generated, and the surface model was exported as a point cloud.

4.2.3. Surface Reconstruction

An open source meshing package, MeshLab, was used to import and process the point cloud exported from Slicer3D. The marching cubes algorithm [59], a robust surface reconstruction algorithm commonly used in medical applications, was selected and used on the point cloud. The resulting surface reconstruction did not result in a usable geometry and exhibited substantial error. Many features of the pulmonary vasculature were rendered along with the airways. Extensive manual cleanup was required to isolate the surfaces of the airways. The resulting surface reconstruction can be seen in Figure 4.1.

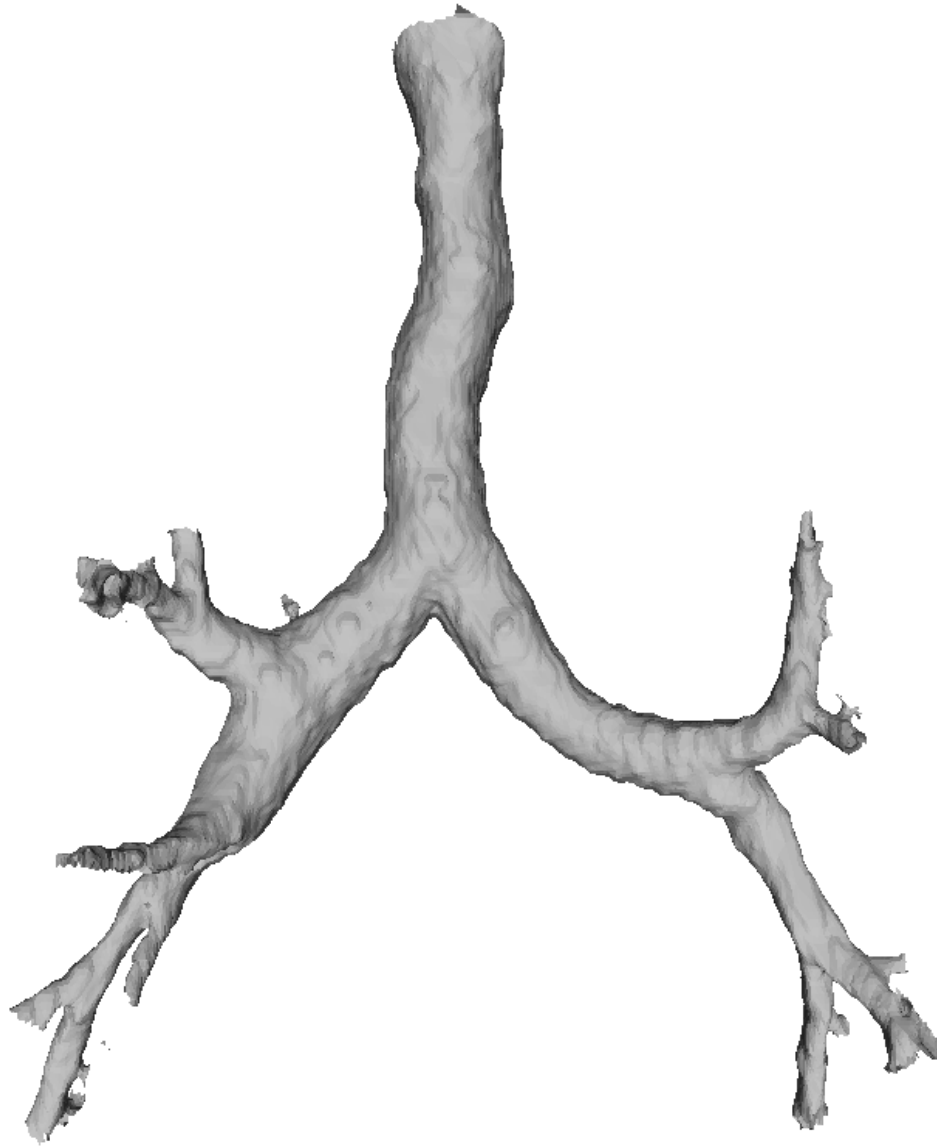


Figure 4.1

A 9-generation surface reconstruction of the pulmonary airways from a set of standard resolution CT images after cleaning of erroneous surfaces.

4.3. Mesh Generation

The effects of mesh quality on solutions for steady flow through a CT-based airway geometry have not been examined, however, structured meshes are preferable for idealized airway models. Consequently, several mesh topologies were explored during mesh generation. Initially a structured surface mesh was generated to leave open the possibility of completing an entirely structured mesh.

4.3.1. Structured Surface Mesh

The generation of the structured surface mesh for a viable blocking topology required a minimum of four domains at each axial cross section. Between generations domains had to rotate 0° to 90° to be properly orientated to diverge at the next bifurcation.

The quality of the database also presented a problem while generating the surface mesh. Erroneous nodes and non-physical features were identified and corrected. This manual manipulation of the database was required to maintain a consistent quality and to allow for an acceptable mesh quality. A structured surface mesh was generated for all nine generations and can be seen in Figure 4.2.

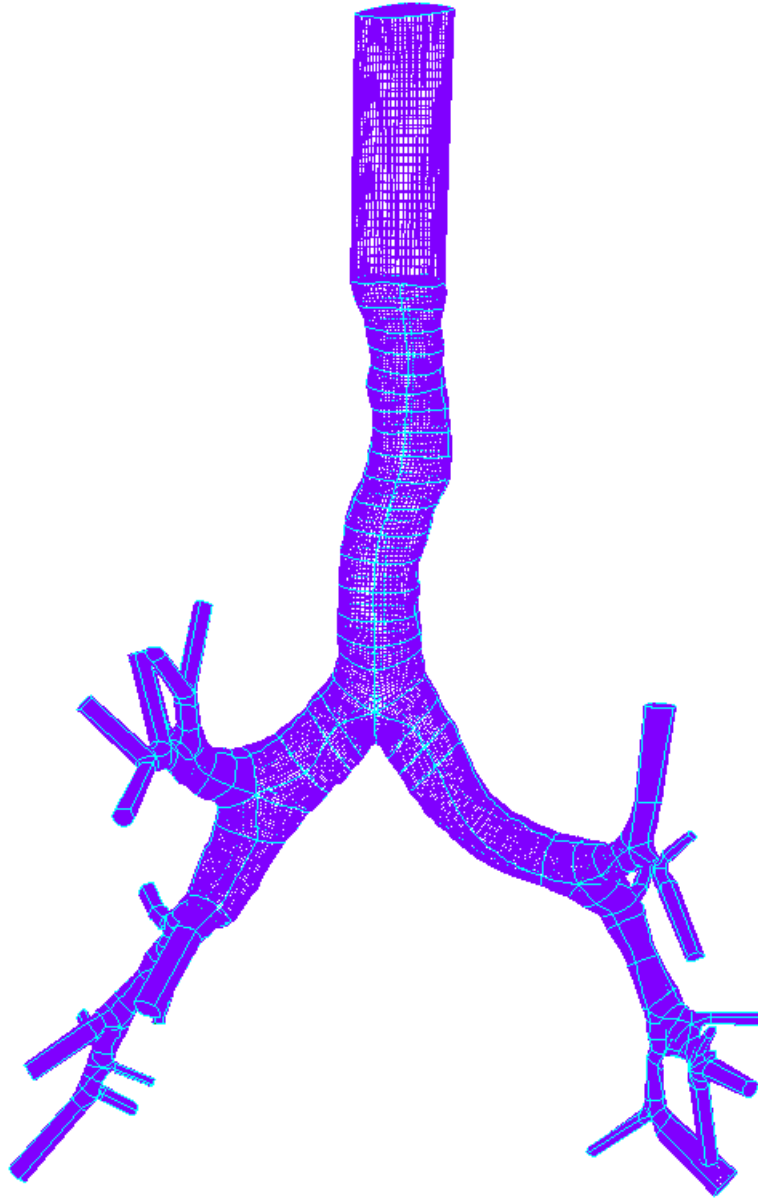


Figure 4.2

A structured surface mesh and 625k node hybrid mesh generated from a 9-generation surface reconstruction of a set of standard resolution CT images.

4.3.2. Hybrid Volume Mesh

Following the completion of the surface mesh structured and unstructured boundary layers were generated. Maintaining mesh quality in the structured boundary layer required blocks for each domain to allow for maximum control of node distributions through the severe undulations of the geometry. Extrusion was used to generate an unstructured boundary layer, however, mesh quality was also difficult to control in the unstructured boundary layer also requiring a large number of blocks to accommodate undulations and the variable diameters of the airways.

The structured boundary layer was completed to 3-generations and the unstructured boundary layer was completed to 6-generations. Stable solutions were only obtained through 3-generations and 4-generations with the structured and unstructured boundary layers, respectively.

4.3.3. Distal Airway Extensions

Many of the terminal airways were unable to be rendered further than the preceding bifurcation. Enforcing open boundary conditions at these truncated airways would have non-physical effects on the flow field through the preceding bifurcations. Straight extensions of uniform diameter were added to these nascent airways to allow for the use of a greater number of airways during modeling. This technique has precedent [23] and is particularly important for modeling complete flow reversal to allow for fully developed flow to enter the completely resolved airways.

CHAPTER 5

PULMONARY AIRFLOW MODELS

In this chapter results from cases run on the CT-based airway geometry are presented and discussed. The steady solutions are described first, followed by the unsteady solutions. Comparisons are made between the two. Finally, results from particle cases are presented and compared.

5.1. Steady Flow

Steady flow solutions were obtained for Reynolds numbers of approximately 875 and 1750 through the trachea. The flow rates for each of these cases were intended to approximate the unsteady solutions at peak inspiration for Womersley numbers of $\alpha = 4.72$ and $\alpha = 6.68$, respectively. These cases used lobar-specific boundary conditions to generate the physiologically appropriate flow rates through each lobar bronchus. These steady solutions were for inspiration – steady solutions were not obtained for expiratory flow.

For the lower Reynolds number case the residual was driven to the order of machine epsilon in fewer than 2500 iterations. Six cross sections were identified; one in the trachea and one in each of the lobar bronchi. Volumetric flow rates were computed

at each of these cross sections. All flow rates measured deviated no more than 0.25% from the targeted values.

For the higher Reynolds number case the residual was driven to the order of machine epsilon over 12000 iterations. Again, six volumetric flow rates were computed at cross sections in the trachea and lobar bronchi. All flow rates measured deviated no more than 1.0% from the targeted values.

New cross sections, near the cross sections used for measuring flow rates and close to the midpoint of each lobar bronchus, were created for analysis of secondary flows. A large number of three-dimensional velocity vectors were projected onto these cross sections to visualize the secondary flows. Consequently, these vectors still include a component of velocity normal to the cutting plane. These cross sections were oriented orthogonal to the axial flow as much as possible to best elucidate the secondary flow features.

Identifying cutting planes for each of these cross sections was not straightforward. Given the complexity of the geometry – undulations, varying curvature, and varying cross sections – creating a cutting plane orthogonal to axial flow was non-trivial. In some cases cutting planes were identified which clearly depict vorticity, vortices, and secondary flow phenomena as desired. In other cases vorticity and vortices were clearly depicted in regions of the cross section while in other regions of the cross section secondary flows were indicative of motion toward geometry features downstream. Cutting planes for cross sections were identified in each lobar

bronchus that, for both Reynolds numbers, exhibited clearly visible vorticity. These cross sections are shown with abbreviated labels in Figure 5.2.

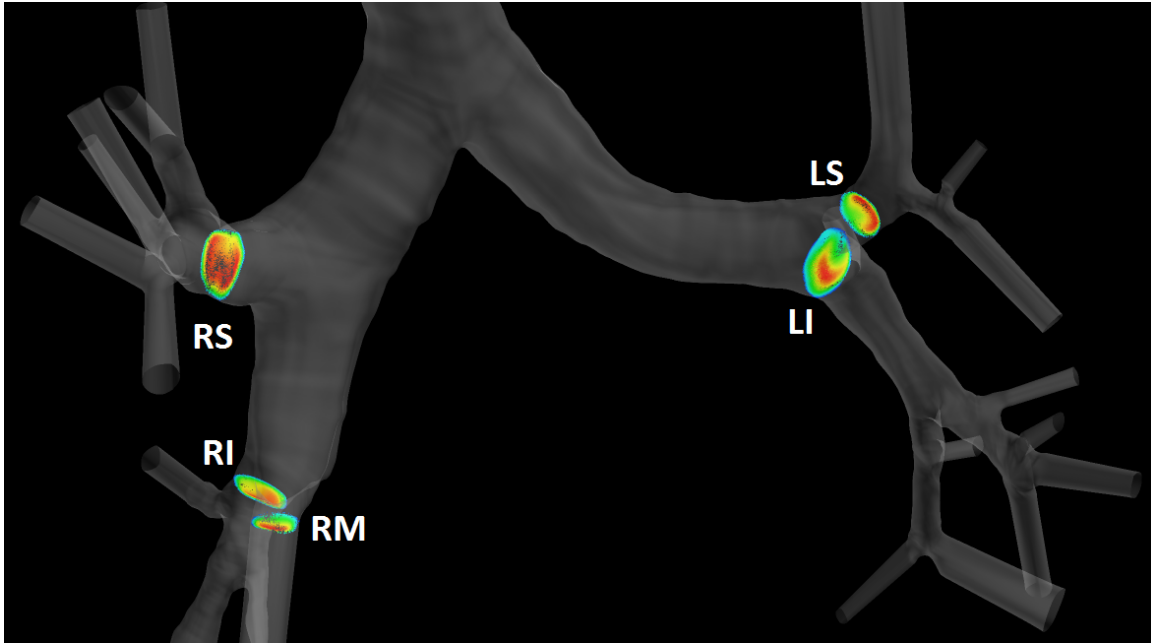


Figure 5.1

Cross-sections from each lobar bronchus orthogonal to the axial flow. These cross sections are labeled by the lobar bronchi; RS (right superior), RM (right middle), RI (right inferior), LS (left superior), and LI (left inferior).

5.2. Unsteady Flow

Unsteady flow solutions were obtained for tidal breathing at two Womersley numbers, $\alpha = 4.72$ and $\alpha = 6.68$, for periods of $T = 8\text{s}$ and $T = 4\text{s}$. The flow rates enforced were selected to induce the physiologically appropriate change in volume for each lobe during tidal breathing. As noted, the parameters for the steady cases were set to approximate the flow conditions at peak inspiration for each of these cases.

Each of these solutions was run for five complete breathing cycles. 96 data sets were recorded for each breathing cycle at phase angles of $\pi/48$ radians (3.75°). 7,968 iterations were run per respiratory cycle for both Womersley numbers. Volumetric flow rates were measured through the trachea and through each lobar bronchus in the same manner as in the steady flow solutions. For the $\alpha = 4.72$ case the volume flux for each cycle deviated no more than 0.25% from the targeted value. A deviation of no more than 0.25% was observed between the initial cycle and subsequent cycles. For the $\alpha = 6.68$ case the volume flux for each cycle deviated no more than 1.0% from the targeted value. A deviation of no more than 0.5% was observed between the initial cycle and subsequent cycles.

A total of twenty-six cross-sections were defined in order to visualize the flow through animation. Each of these cross sections was roughly orthogonal to the axial flow and three-dimensional vectors were placed to aid in frame-by-frame visualization. An animation was created comprised of 96 frames per cycle, one from each recorded data set. Figure 5.1 shows 9 frames of the animation for the $\alpha = 4.72$ case, from 0 to 2π

at intervals of $\pi/4$ (0° - 360° at intervals of 45°). This respiratory cycle covers a time of 8 seconds.

The animation depicted in Figure 5.1 illustrated the oscillatory nature of the flow but did little to shed light on flow features. Velocity vector projections onto the cross-sections previously identified for steady flow solutions were created for each lobar bronchus in the unsteady solutions. For the unsteady flow three phase angles were rendered at each cross section. These phase angles of $\pi/6$, $\pi/3$, and $\pi/2$ were representative of inspiration from 50% \bar{V}_{\max} to \bar{V}_{\max} .

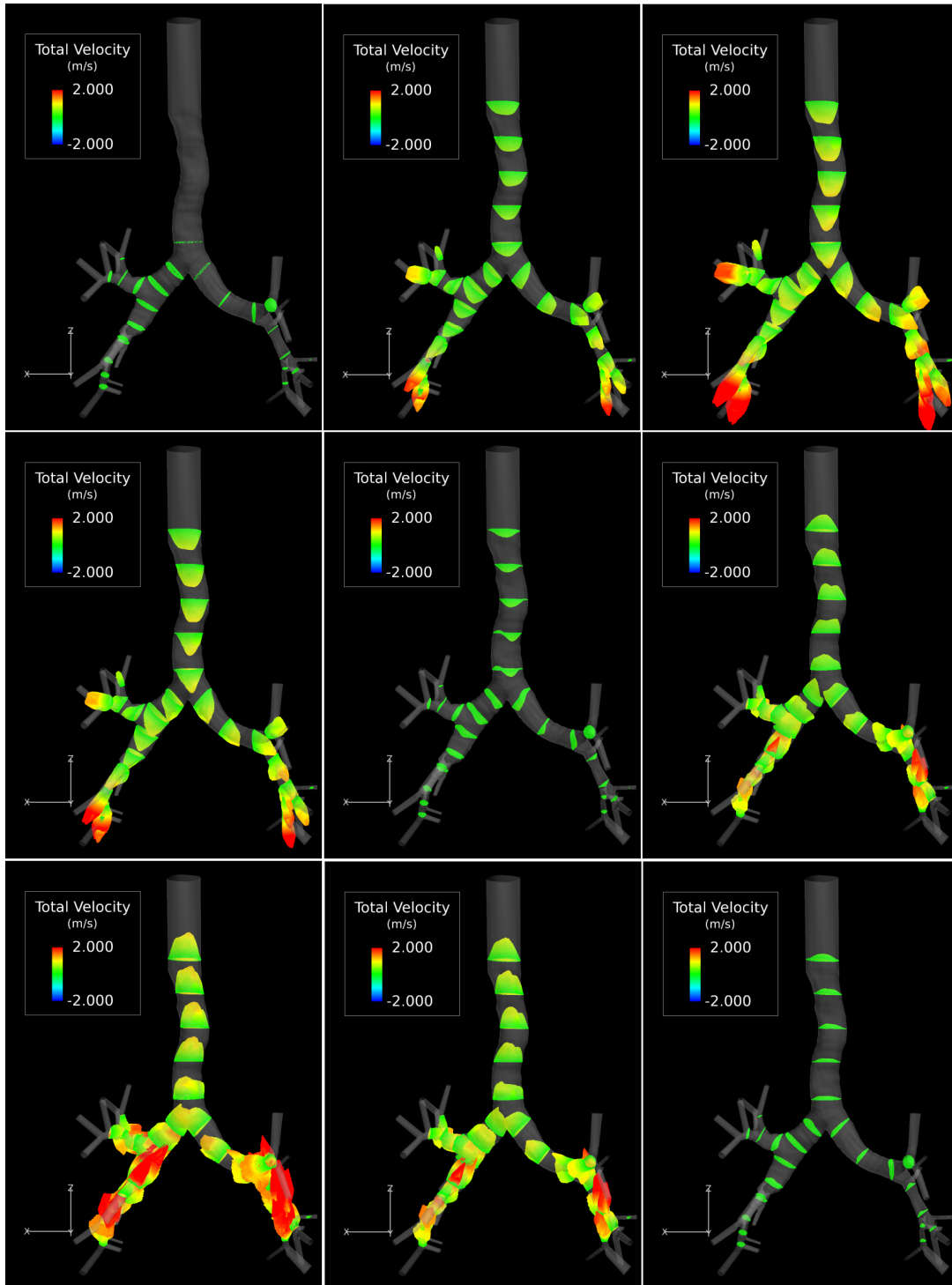


Figure 5.2

A numerical solution from *Tenasi* for a complete breathing cycle from rest. This solution is for tidal breathing at $\alpha = 4.72$ (phase angles are shown from 0° to 360° at 45° intervals).

At \bar{V}_{\max} flow rates are approximately equal to those in the steady solutions, as intended. This enables a direct comparison of secondary flows in the steady and unsteady solutions. The cross sections for comparison of secondary velocities are depicted and labeled in Figure 5.2. Upon comparison of solutions from the steady case of $Re = 875$ and the unsteady case of $\alpha = 4.72$, the secondary flows at cross-sections from each lobar bronchus were approximately equal. This is illustrated in Figure 5.3, which depicts the comparison of the steady solution and unsteady solution at peak inspiration in the cross section in the left inferior lobar bronchus. For the $\alpha = 6.68$ case, the secondary flows at cross sections in each lobar bronchus exhibited discernable differences. The most prominent differences were apparent in the right superior lobar bronchus, seen in Figure 5.4.

The local Reynolds number for the left inferior bronchus at peak inspiration and $\alpha = 4.72$ is approximately 500. Local Reynolds numbers at the cross-sections selected for secondary flow analysis, for the right superior, right middle, right inferior, and left superior bronchi, are approximately 400, 240, 580, and 450, respectively. Thus, for tidal breathing at $\alpha = 4.72$ all flow through the lobar bronchi is laminar.

The local Reynolds number for flow through the right superior bronchus at peak inspiration in the $\alpha = 6.68$ case is approximately 800. Local Reynolds numbers at the cross-sections selected for secondary flow analysis, for the right middle, right inferior, left superior, and left inferior bronchi, are approximately 480, 1160, 900, and 1000, respectively. Thus, for tidal breathing at $\alpha = 6.68$ all flow through the lobar bronchi is also laminar.

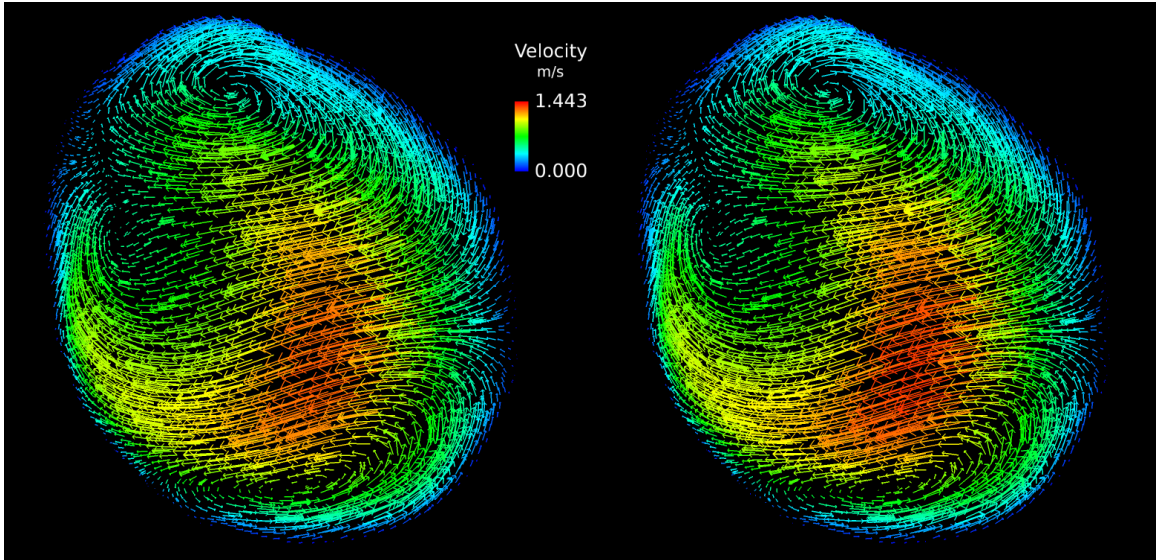


Figure 5.3

A comparison of secondary flows in an unsteady solution at $\alpha = 4.72$ (left) and $\alpha = 4.72$ with a steady solution for $Re = 875$ (right) in the left inferior lobar bronchus.

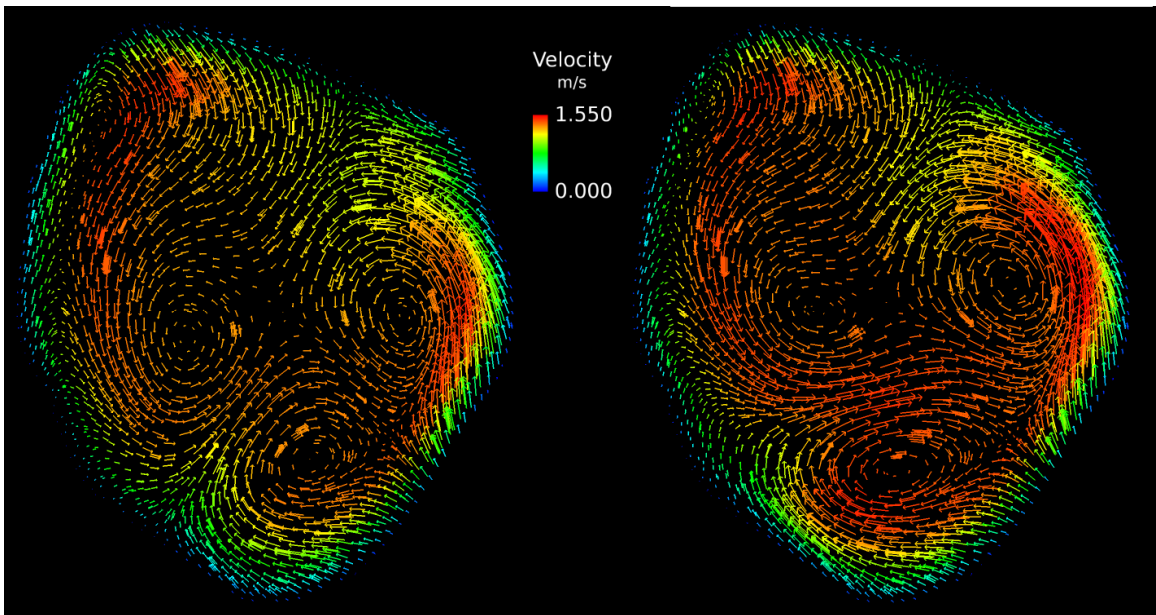


Figure 5.4

A comparison of secondary flows in an unsteady solution at $\alpha = 6.68$ (left) and $\alpha = 6.68$ with a steady solution for $Re = 1750$ (right) in the right superior bronchus.

Comparisons of secondary flows over increasing phase angles during inspiration were conducted for each of the five lobar bronchi. For the $\alpha = 4.72$, three exhibited notable development of secondary flow features during the acceleration of inhalation. Comparisons of secondary flows through these three lobar bronchi, the left inferior, right middle, and right superior, can be seen in Figure 5.5, Figure 5.6, and Figure 5.7, respectively. In these figures, secondary flow features are shown for phase angles of $\phi = \pi/6$, $\phi = \pi/3$, and $\phi = \pi/2$, increasing from left to right. These phase angles correspond to an increase in mean velocity from $0.5 \bar{V}_{\max}$ to \bar{V}_{\max} (i.e. peak inspiration). For the $\alpha = 4.72$ case, with a period of $T = 8s$, these phase angles correspond to times of $t = 0.6\bar{6}s$, $t = 1.3\bar{3}s$, and $t = 2.0s$.

In each of the figures depicting secondary flow evolution, vorticity can be seen increasing. As the phase angle increases, vorticity in existing vortices becomes more pronounced and new flow features indicative of vorticity appear. In Figure 5.5 two weak vortices experience increasing vorticity and both shift toward the airway walls. In this figure a third flow feature appears at $\phi = \pi/3$ but fails to develop into a fully defined vortex in the plane depicted. In Figure 5.6 no vorticity is present at $\phi = \pi/6$, however, two flow features appear at $\phi = \pi/3$ and become more defined at $\phi = \pi/2$. These features fail to fully develop into vortices in the plane rendered. In Figure 5.7 two significant flow features are present at $\phi = \pi/6$. These features shift slightly toward airway walls and exhibit increased vorticity at $\phi = \pi/3$, becoming two weak vortices. At $\phi = \pi/2$, four flow features are observed, three of which are weak vortices, along with further shifts of the previous features.

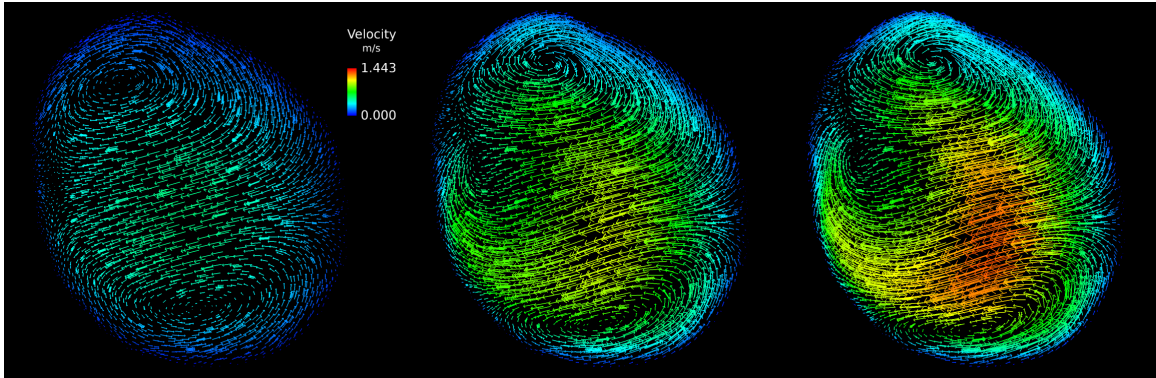


Figure 5.5

A comparison of secondary flows into the left inferior bronchus at , , and .

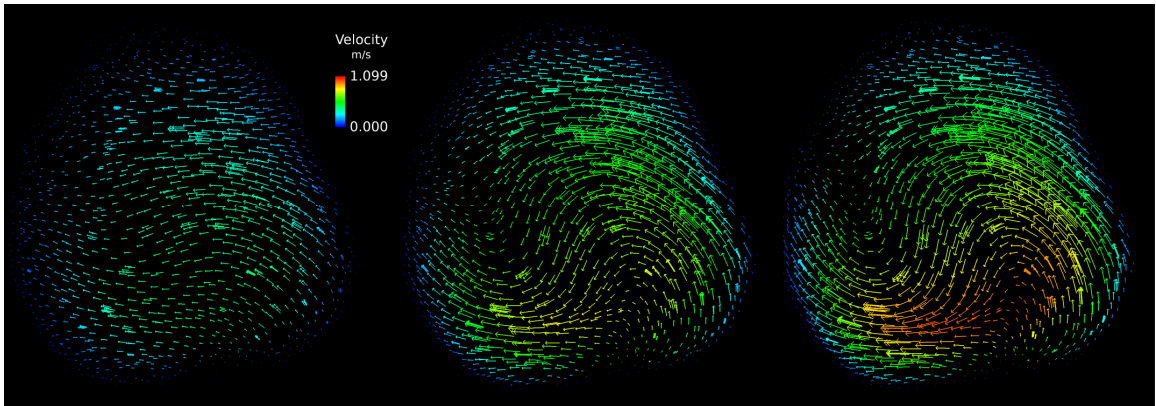


Figure 5.6

A comparison of secondary flows into the right middle bronchus at , , and .

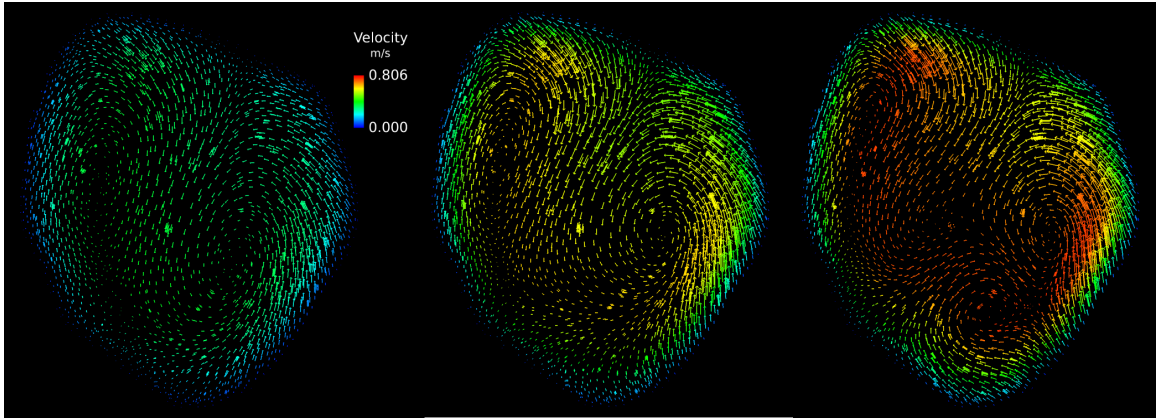


Figure 5.7

A comparison of secondary flows into the right superior bronchus at , , and .

When comparing the evolution of secondary flows between the $\alpha = 4.72$ case and the $\alpha = 6.68$ case it is important to note that the mean velocity at $\phi = \pi/2$ in the $\alpha = 4.72$ case is roughly equal to the mean velocity at $\phi = \pi/6$ in the $\alpha = 6.68$ case. Thus, if the development of secondary flow features was solely dependent on the flow rate and Reynolds number, flow features at $\phi = \pi/2$ in the $\alpha = 4.72$ case should be of the same form as flow features at $\phi = \pi/6$ in the $\alpha = 6.68$ case. This was not the case.

For the $\alpha = 6.68$ case, secondary flows through the left inferior bronchus, the right middle bronchus, and the right superior bronchus can be seen at three phase angles in Figure 5.8, Figure 5.9, and Figure 5.10, respectively. These figures appear very similar to Figure 5.5, Figure 5.6, and Figure 5.7 previously presented. Note the significant changes in the velocity magnitude apparent in the figures' legends.

Given the similarities of Figure 5.5 and Figure 5.8, Figure 5.6 and Figure 5.9, and Figure 5.7 and Figure 5.10, clearly, the evolution of secondary flow features in cases for both Womersley numbers is analogous. In general, secondary flow features in the $\alpha = 6.68$ case, at the phase angles observed, were more defined and exhibited greater degrees of vorticity than the same features observed in the $\alpha = 4.72$ case. Furthermore, the same features are present at the corresponding phase angles in the respective lobar bronchi for both Womersley numbers – neither case exhibits flow features not present in the other. The appearance of new flow features can be observed at the same phase angles in cases for both Womersley numbers.

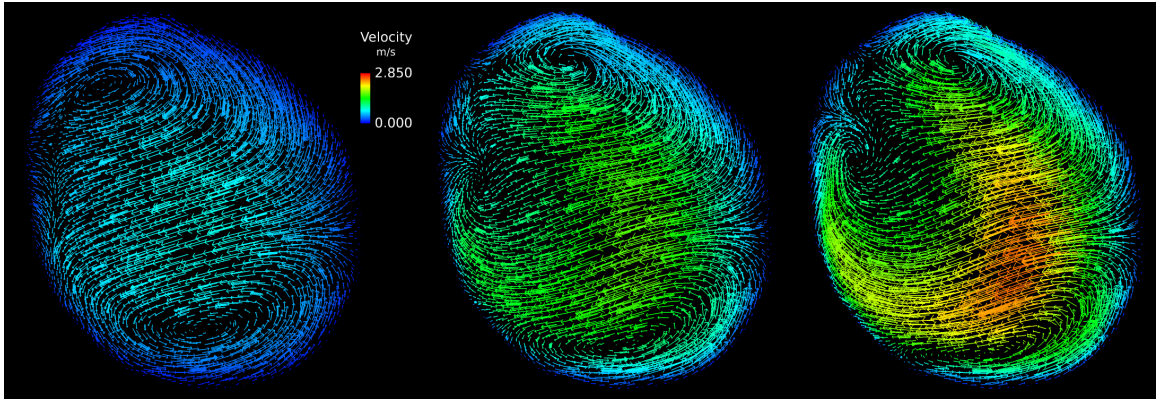


Figure 5.8

A comparison of secondary flows into the left inferior bronchus at $\theta = 0^\circ$, 45° , and 90° .

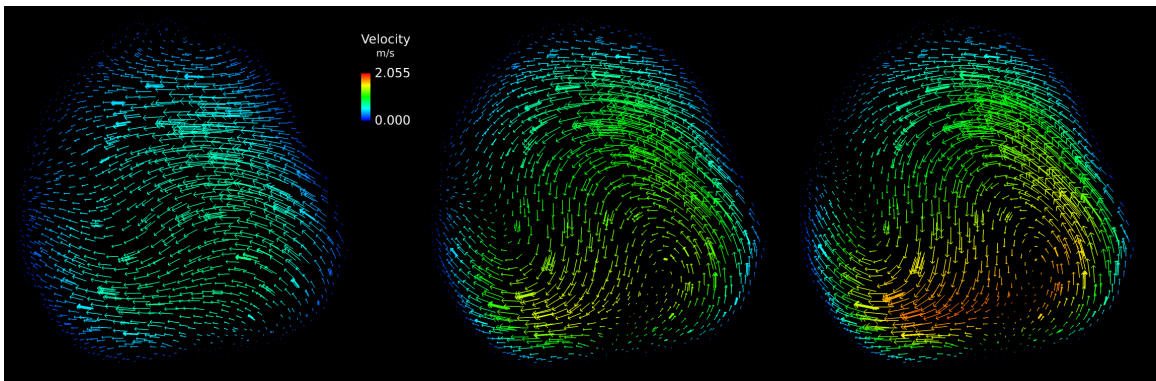


Figure 5.9

A comparison of secondary flows into the right middle bronchus at $\theta = 0^\circ$, 45° , and 90° .

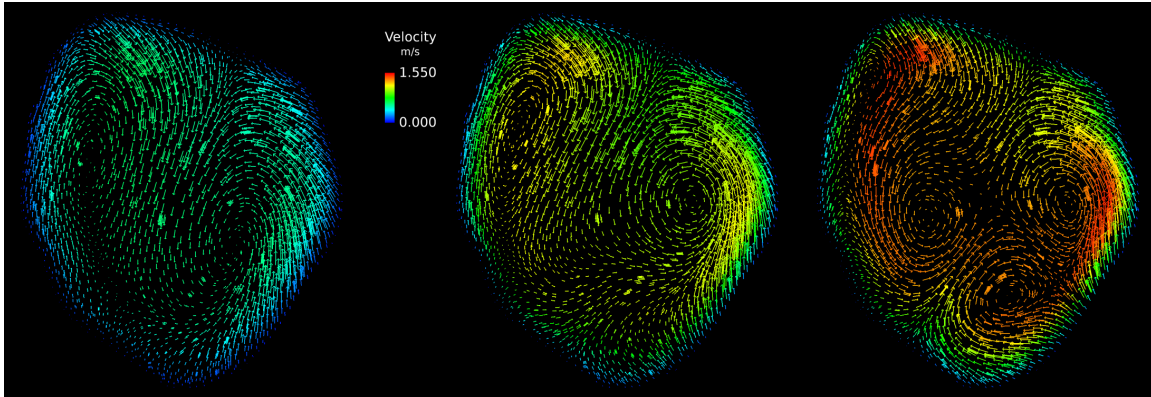


Figure 5.10

A comparison of secondary flows into the right superior bronchus at $Re = 100$, $Re = 200$, and $Re = 400$.

The two most significant differences between the cases for the two Womersley numbers are the flow rates and the acceleration of the flow. Velocity does not appear to play a role in the observed flow features, however.

5.3. Particle Transport

Eight cases were run to model particle transport for each of the resting breathing rates being examined. Four cases were run for each Womersley number, two of which were steady solutions and two of which were unsteady solutions. For each of these pairs, one case was run ignoring the hygroscopic effects of the particles while the other was run modeling the hygroscopic effects of particles. Each of these cases modeled 1000 particles distributed randomly over a square region circumscribing a cross section at the proximal end of the trachea. This same distribution was used to specify particle release points for each of the eight cases.

For each case 835 of the 1000 particles fell into the computational geometry. Since particles were released from a region circumscribing the trachea, particles depositing in the trachea were ignored. Particles depositing at the region of bifurcation in the trachea and beyond were counted. This was intended to mitigate the impact of particles released in the boundary layer, very near the undulating airway walls, on deposition analysis. This was due to the observation that a significant number of particles were depositing within a very short distance of their release.

The deposition fraction (DF) is a typical metric used in the analysis of pharmaceutical aerosol transport. It is defined

$$DF = \frac{\text{number of particles deposited}}{\text{number of particles released}} \times 100\%$$

As the study is concerned with regional flow rates, deposition fractions were assessed regionally. In order to examine the effects of steady and unsteady solutions on particle

trajectory the regional distributions of the final locations of particles were computed. These distributions were computed by keeping track of the total number of particles that passed through each lobar bronchus. The pre-lobar and lobar regions examined were bound by the carinal ridge and the ridges of bifurcation of each lobar bronchus. Table 5.1 and Table 5.2 show data for regional deposition fractions and distributions of final particle locations for the $\alpha = 4.72$ steady and unsteady cases, respectively.

Table 5.1 and Table 5.2 contain data summarizing the regional trajectories of particles modeled at $\alpha = 4.72$. The effects of hygroscopy are not particularly significant for either steady or unsteady solutions. Substantial differences, however, are seen comparing the results of steady and unsteady particle solutions.

Differences between steady and unsteady particle solutions can be seen foremost in total deposition fractions. Roughly 20% less particles were deposited in the airways in the unsteady particle cases. Notably, deposition in the pre-trachea airways for unsteady cases is negligible in contrast to the ~5% of particles deposited in the same region in steady cases.

Table 5.1 Deposition fraction and final particle location data from steady particle transport models with and without the effects of hygroscopy, $\alpha = 4.72$.

	steady flow			
	no hygroscopic effects		with hygroscopic effects	
	DF	total particles	DF	total particles
G1 to lobar bronchi	5.64%	5.64%	5.08%	5.08%
right superior	18.74%	27.00%	18.12%	26.86%
right middle	*	9.04%	*	9.13%
right inferior	18.35%	25.03%	18.25%	25.03%
left superior	3.67%	14.02%	3.65%	14.47%
left inferior	14.02%	19.27%	13.43%	19.43%
Total	60.42%	100.00%	58.54%	100.00%

Table 5.2 Deposition fraction and final particle location data from unsteady particle transport models with and without the effects of hygroscopy, $\alpha = 4.72$.

	unsteady flow			
	no hygroscopic effects		with hygroscopic effects	
	DF	total particles	DF	total particles
G1 to lobar bronchi	0.87%	0.87%	0.75%	0.75%
right superior	14.73%	27.84%	14.13%	27.75%
right middle	*	8.24%	*	8.38%
right inferior	9.24%	22.10%	8.50%	21.63%
left superior	3.62%	12.36%	4.00%	12.38%
left inferior	11.86%	28.59%	12.25%	29.13%
Total	40.32%	100.00%	39.63%	100.00%

Further examination of Table 5.1 and Table 5.2 indicates major deviations of particle trajectories. The most pronounced instance of this can be seen in a ~10% increase in overall particles in the unsteady case ultimately ending up in the left inferior lobe. Noteworthy deviations in final particle locations between steady and unsteady cases are also seen in the right inferior and left superior lobes.

Table 5.3 and Table 5.4 show data for regional deposition fractions and distributions of final particle locations for the $\alpha = 6.68$ steady and unsteady cases, respectively. The data contained in these tables summarizes the regional trajectories and deposition of the particles modeled. Again, hygroscopic effects are not significant. A comparison of all hygroscopic cases and identical non-hygroscopic cases indicated a deviation of less than 2% for all regions. The maximum deviation between total DFs for the same cases was also less than 2%. These observations of the hygroscopic effects of particles on trajectory and deposition fraction is not statistically significant due to the low sample size of particles. However, even with the low sample size, it is significant that there was deviation present in 47 of 48 measures of comparison present in Table 1, Table 2, Table 3, and Table 4. The effects of modeling hygroscopic properties of particles may indeed be significant in particles that are more hygroscopic than NaCl.

As for $\alpha = 4.72$, DFs were significantly different in the steady and unsteady cases. The deviation between steady and unsteady for $\alpha = 6.68$ cases was even more pronounced, with roughly 37% more particles depositing in steady cases. DFs in the pre-lobar regions were substantial in steady cases with roughly 20% of particles depositing prior to entering the lobar bronchi. In unsteady cases the number of particles depositing prior to entering the lobar bronchi was again minimal, with DFs a little greater than 1%. As for $\alpha = 4.72$, regional distributions of particles varied greatly between steady and unsteady cases.

Table 5.3 Deposition fraction and final particle location data from steady particle transport models with and without the effects of hygroscopy, $\alpha = 6.68$.

	steady flow			
	no hygroscopic effects		with hygroscopic effects	
	DF	total particles	DF	total particles
G1 to lobar bronchi	21.03%	21.03%	19.73%	19.73%
right superior	18.39%	23.02%	18.53%	23.07%
right middle	*	7.01%	*	7.60%
right inferior	21.96%	22.75%	21.73%	22.53%
left superior	5.82%	12.04%	5.47%	11.73%
left inferior	13.49%	14.15%	14.93%	15.33%
Total	80.69%	100.00%	80.40%	100.00%

Table 5.4 Deposition fraction and final particle location data from unsteady particle transport models with and without the effects of hygroscopy, $\alpha = 6.68$.

	unsteady flow			
	no hygroscopic effects		with hygroscopic effects	
	DF	total particles	DF	total particles
G1 to lobar bronchi	1.51%	1.51%	1.01%	1.01%
right superior	15.70%	26.13%	15.49%	26.57%
right middle	*	10.55%	*	10.33%
right inferior	8.29%	22.24%	8.69%	22.54%
left superior	3.14%	13.44%	3.15%	14.11%
left inferior	13.82%	26.13%	14.74%	25.44%
total	42.46%	100.00%	43.07%	100.00%

CHAPTER 6

CONCLUSIONS

Flow through the pulmonary airways at resting breathing rates is strictly laminar for typical tidal volumes, with Reynolds numbers remaining below 2000. Moreover, flow through the lobar bronchi exhibit Reynolds numbers substantially lower than the Reynolds number observed in the trachea. This laminar flow through the lobar bronchi, however, exhibits complex flow features in cases of both steady and unsteady flows.

Weak vorticity is present in the trachea during both steady and unsteady inspiratory cases. As inspiratory flow through the trachea is not preceded by any bifurcations this weak vorticity results from the slight curvature of the trachea. This underscores the significant effects of the complexity of the geometry on secondary flow features in real pulmonary airflow.

Complex flow phenomena were observed in both steady and unsteady flows at all sections selected for analysis. In the unsteady cases such features developed with time. Comparing the development of these features in the $\alpha = 4.72$ and $\alpha = 6.68$ cases indicates that this development has a greater dependence on time than velocity.

A comparison of the $\alpha = 4.72$ case at $\varphi = \pi/2$ with the $Re = 875$ case showed good agreement for all cross sections examined. This was as expected since the latter case

was intended to approximate the former. Thus, at Reynolds numbers below 1000 steady solutions appear to be good approximations of transient solutions.

A comparison of the $\alpha = 6.68$ case at $\varphi = \pi/2$ and the $Re = 1750$ case did not lead to the same conclusion. Noticeable differences were present between the two cases. These differences were not substantial, however, they were non-trivial.

A general comparison of the $\alpha = 4.72$ and $Re = 875$ cases with the $\alpha = 6.68$ and $Re = 1750$ cases showed some noteworthy differences. Comparing the three increasing phase angles for each unsteady case revealed a higher degree of vorticity and more developed flow features in the $\alpha = 6.68$ case. This was the case despite the development of flow features in both cases being similar with respect to phase angle. A higher degree of vorticity and more developed flow features were also observed in the $Re = 1750$ case upon comparison with the $Re = 875$ case.

The hygroscopic effects of NaCl particles were not significant for any of the four cases run for comparison. Effects of the hygroscopic properties of NaCl were, however, observed in each of the four comparisons. This observation does not necessarily extend to all particles. The effects of hygroscopy are dependent on the hygroscopic properties of the type of particles being modeled.

No conclusions could be made regarding the effects of inhalation transience on particle trajectory through the airways. Furthermore, no conclusions can be made regarding the effects of Womersley and Reynolds numbers on particle trajectory. Observations from the results are insignificant due to the small sample size of particles used in this study.

Inhalation transience has a significant effect on deposition fractions of NaCl particles in laminar flow through the airways. Specifically, inhalation transience reduces the number of particles deposited in early generations of the airways allowing for a greater number of particles to travel further toward the conduction zone of the lungs.

CHAPTER 7

FUTURE WORK

This work has significant limitations. The exclusion of the upper airways in the computational geometry forces the approximation of uniform flow entering the trachea. This is a non-physical approximation as flow entering the trachea passes through the laryngeal jet, a complex morphological feature that introduces complex flow features to flow entering the trachea. Moreover, the truncated computational geometry limits the region for particle release to inside the trachea rather than at the mouth. The release of particles from a point within the trachea is not an ideal model for studying airborne contaminant inhalation or pharmaceutical aerosol transport. Future work should include either an idealized upper airway model or a patient-specific upper airway model.

Another limiting factor was the number of cases run. Only two breathing rates were modeled. Moreover, these breathing rates were driven by idealized, non-physical transient inhalation waveforms. The breathing rates modeled restricted solutions to laminar flow conditions. Future work should examine flow at high Womersley numbers and flow rates typical of active breathing rates. Furthermore, inhalation waveforms better approximating natural inhalation dynamics should be considered. Inhalation waveforms should be examined closely when modeling pharmaceutical aerosol delivery.

Particle models were limited by the variety of particles selected for modeling. Future work should consider a variety of particles representative of airborne contaminants and pharmaceutical aerosols. Particles exhibiting more pronounced hygroscopic effects should also be examined.

This study did not address the effects of airway motion on flow and particle transport. Future work should examine the effects of idealized airway motion and patient-specific airway motion. The use of time-dependent sets of CT images should be used in future work for the modeling of patient-specific airway motion.

The quality of the image processing and geometry generation is also something that should be considered in future work. High-resolution CT imagery and computational geometries with greater than 25 distal airways should be used for future work. A greater number of resolved airways present in the geometry could allow for bronchopulmonary specific boundary conditions.

Doctor and medical researchers are often interested in diseased airways. A variety of CT-based airway models, including those exhibiting pronounced features of diseased airways, should be examined with the techniques described in this study. The effects of respiratory illnesses can also affect regional flow rates. Thus, regional flow rates reflecting the effects of respiratory illnesses should be considered as well.

Particle sample size should be increased so as to yield statistically significant data regarding the particle trajectory and local deposition fractions.

The mesh quality used in the airway geometry was not thoroughly examined. Mesh convergence tests should be conducted with hybrid meshes of increasing node

density. Viscous boundary layers should also be considered. Particular attention should be given to the affect of these mesh factors on secondary flows. As entirely structured meshes have shown good results in idealized airway models the generation of structured meshes in CT-based geometries should be explored.

REFERENCES

1. Weibel, E.R., *Geometry and dimensions of airways of conductive and transitory zones*. 1963: Springer.
2. Horsfield, K. and G. Cumming, *Morphology of the bronchial tree in man*. 1968.
3. Horsfield, K. and G. Cumming, *Angles of branching and diameters of branches in the human bronchial tree*. *The Bulletin of mathematical biophysics*, 1967. **29**(2): p. 245-259.
4. Horsfield, K., et al., *Models of the human bronchial tree*. *J. appl. Physiol*, 1971. **31**(2): p. 207-217.
5. Olson, D.E., *Fluid Mechanics Relevant to Respiration Flow Within Curved or Elliptical Tubes and Bifurcation Systems*. 1971, Imperial College London.
6. Hammersley, J.R. and D.E. Olson, *Physical models of the smaller pulmonary airways*. *J. Appl. Physiol*, 1992. **72**(6): p. 2402-2414.
7. Heistracher, T. and W. Hofmann, *Physiologically realistic models of bronchial airway bifurcations*. *Journal of Aerosol Science*, 1995. **26**(3): p. 497-509.
8. Fresconi, F.E. and A.K. Prasad, *Secondary velocity fields in the conducting airways of the human lung*. *Journal of biomechanical engineering*, 2007. **129**(5): p. 722-732.
9. Fresconi, F.E., A.S. Wexler, and A.K. Prasad, *Expiration flow in a symmetric bifurcation*. *Experiments in fluids*, 2003. **35**(5): p. 493-501.
10. Theunissen, R. and M.L. Riethmuller, *Particle image velocimetry in lung bifurcation models*, in *Particle Image Velocimetry*. 2008, Springer. p. 73-101.
11. Ma, B., et al., *CFD simulation and experimental validation of fluid flow and particle transport in a model of alveolated airways*. *Journal of aerosol science*, 2009. **40**(5): p. 403-414.

12. Tanaka, G., et al., *Spatial and temporal variation of secondary flow during oscillatory flow in model human central airways*. Journal of biomechanical engineering, 1999. **121**(6): p. 565-573.
13. Ramuzat, A. and M.L. Riethmuller. *PIV investigation of oscillating flows within a 3D lung multiple bifurcations model*. in *11th International Symposium on Applications of Laser Techniques to Fluid Flows, Lisbon, Portugal, July*. 2002.
14. Pedley, T.J., R.C. Schroter, and M.F. Sudlow, *The prediction of pressure drop and variation of resistance within the human bronchial airways*. Respiration physiology, 1970. **9**(3): p. 387-405.
15. Pedley, T.J., R.C. Schroter, and M.F. Sudlow, *Energy losses and pressure drop in models of human airways*. Respiration physiology, 1970. **9**(3): p. 371-386.
16. Pedley, T.J., R.C. Schroter, and M.F. Sudlow, *Flow and pressure drop in systems of repeatedly branching tubes*. Journal of Fluid Mechanics, 1971. **46**(02): p. 365-383.
17. Pedley, T.J., M.F. Sudlow, and J. Milic-Emili, *A non-linear theory of the distribution of pulmonary ventilation*. Respiration physiology, 1972. **15**(1): p. 1-38.
18. Pedley, T.J., *Pulmonary fluid dynamics*. Annual Review of Fluid Mechanics, 1977. **9**(1): p. 229-274.
19. Womersley, J.R., *Method for the calculation of velocity, rate of flow and viscous drag in arteries when the pressure gradient is known*. The Journal of physiology, 1955. **127**(3): p. 553-563.
20. Yung, C.-N., K.J. De Witt, and T.G. Keith, *Three-dimensional steady flow through a bifurcation*. Journal of biomechanical engineering, 1990. **112**(2): p. 189-197.
21. Gradon, L. and D. Orlicki, *Deposition of inhaled aerosol particles in a generation of the tracheobronchial tree*. Journal of aerosol science, 1990. **21**(1): p. 3-19.
22. BalÁshÁZy, I., T. Heistracher, and W. Hofmann, *Air flow and particle deposition patterns in bronchial airway bifurcations: the effect of different CFD models and bifurcation geometries*. Journal of Aerosol Medicine, 1996. **9**(3): p. 287-301.
23. Van Ertbruggen, C., C. Hirsch, and M. Paiva, *Anatomically based three-dimensional model of airways to simulate flow and particle transport using*

- computational fluid dynamics*. Journal of Applied Physiology, 2005. **98**(3): p. 970-980.
24. Perzl, M.A., et al., *Reconstruction of the lung geometry for the simulation of aerosol transport*. Journal of Aerosol Medicine, 1996. **9**(3): p. 409-418.
 25. Nowak, N., P.P. Kakade, and A.V. Annapragada, *Computational fluid dynamics simulation of airflow and aerosol deposition in human lungs*. Annals of biomedical engineering, 2003. **31**(4): p. 374-390.
 26. Tawhai, M.H., A.J. Pullan, and P.J. Hunter, *Generation of an anatomically based three-dimensional model of the conducting airways*. Annals of biomedical engineering, 2000. **28**(7): p. 793-802.
 27. Longest, P. and L.T. Holbrook, *In silico models of aerosol delivery to the respiratory tract—Development and applications*. Advanced drug delivery reviews, 2012. **64**(4): p. 296-311.
 28. Walters, D.K., et al., *Efficient, physiologically realistic lung airflow simulations*. Biomedical Engineering, IEEE Transactions on, 2011. **58**(10): p. 3016-3019.
 29. Yin, Y., et al., *Simulation of pulmonary air flow with a subject-specific boundary condition*. Journal of biomechanics, 2010. **43**(11): p. 2159-2163.
 30. Rosell, J. and P. Cabras, *A three-stage method for the 3D reconstruction of the tracheobronchial tree from CT scans*. Computerized Medical Imaging and Graphics, 2013. **37**(7): p. 430-437.
 31. Gemci, T., et al., *CFD Simulation of Airflow in a 17-Generation Digital reference model of the human bronchial tree*. J Biomech, 2007. **41**: p. 2047-2054.
 32. Kumar, A., et al. *A graph-based approach to the retrieval of volumetric PET-CT lung images*. in *Engineering in Medicine and Biology Society (EMBC), 2012 Annual International Conference of the IEEE*. 2012. IEEE.
 33. Saksono, P.H., et al., *Computational flow studies in a subject - specific human upper airway using a one - equation turbulence model. Influence of the nasal cavity*. International Journal for Numerical Methods in Engineering, 2011. **87**(1 - 5): p. 96-114.
 34. Gemci, T., et al., *Computational model of airflow in upper 17 generations of human respiratory tract*. Journal of Biomechanics, 2008. **41**(9): p. 2047-2054.
 35. Lin, C.-l., et al., *Computational fluid dynamics*. Engineering in Medicine and Biology Magazine, IEEE, 2009. **28**(3): p. 25-33.

36. Chamoin, L., J.T. Oden, and S. Prudhomme, *A stochastic coupling method for atomic-to-continuum Monte-Carlo simulations*. Computer Methods in Applied Mechanics and Engineering, 2008. **197**(43): p. 3530-3546.
37. Soni, B., D. Thompson, and R. Machiraju, *Visualizing particle/flow structure interactions in the small bronchial tubes*. Visualization and Computer Graphics, IEEE Transactions on, 2008. **14**(6): p. 1412-1427.
38. Longest, P. and S. Vinchurkar, *Effects of mesh style and grid convergence on particle deposition in bifurcating airway models with comparisons to experimental data*. Medical engineering & physics, 2007. **29**(3): p. 350-366.
39. Vinchurkar, S. and P. Longest, *Evaluation of hexahedral, prismatic and hybrid mesh styles for simulating respiratory aerosol dynamics*. Computers & Fluids, 2008. **37**(3): p. 317-331.
40. Tian, G., et al., *Characterization of respiratory drug delivery with enhanced condensational growth using an individual path model of the entire tracheobronchial airways*. Annals of biomedical engineering, 2011. **39**(3): p. 1136-1153.
41. De Backer, J.W., et al., *Validation of Computational Fluid Dynamics in CT-based Airway Models with SPECT/CT 1*. Radiology, 2010. **257**(3): p. 854-862.
42. Balásházy, I., W. Hofmann, and T. Heistracher, *Local particle deposition patterns may play a key role in the development of lung cancer*. Journal of Applied Physiology, 2003. **94**(5): p. 1719-1725.
43. Zhang, Z., C. Kleinstreuer, and C.S. Kim, *Aerosol deposition efficiencies and upstream release positions for different inhalation modes in an upper bronchial airway model*. Aerosol Science & Technology, 2002. **36**(7): p. 828-844.
44. Zhang, Z., C. Kleinstreuer, and Y. Feng, *Vapor deposition during cigarette smoke inhalation in a subject-specific human airway model*. Journal of Aerosol Science, 2012. **53**: p. 40-60.
45. Zhang, Z. and C. Kleinstreuer, *Airflow structures and nano-particle deposition in a human upper airway model*. Journal of computational physics, 2004. **198**(1): p. 178-210.
46. Zhang, Z., et al., *Comparison of micro-and nano-size particle depositions in a human upper airway model*. Journal of aerosol science, 2005. **36**(2): p. 211-233.

47. Li, Z., C. Kleinstreuer, and Z. Zhang, *Particle deposition in the human tracheobronchial airways due to transient inspiratory flow patterns*. Journal of aerosol science, 2007. **38**(6): p. 625-644.
48. Li, Z., C. Kleinstreuer, and Z. Zhang, *Simulation of airflow fields and microparticle deposition in realistic human lung airway models. Part I: Airflow patterns*. European Journal of Mechanics-B/Fluids, 2007. **26**(5): p. 632-649.
49. Li, Z., C. Kleinstreuer, and Z. Zhang, *Simulation of airflow fields and microparticle deposition in realistic human lung airway models. Part II: Particle transport and deposition*. European Journal of Mechanics-B/Fluids, 2007. **26**(5): p. 650-668.
50. Huang, J., et al., *Moving boundary simulation of airflow and micro-particle deposition in the human extra-thoracic airway under steady inspiration. Part I: Airflow*. European Journal of Mechanics-B/Fluids, 2013. **37**: p. 29-41.
51. Mead-Hunter, R., et al., *The influence of moving walls on respiratory aerosol deposition modelling*. Journal of Aerosol Science, 2013. **64**: p. 48-59.
52. Johari, N.H., et al., *Comparative analysis of realistic CT-scan and simplified human airway models in airflow simulation*. Computer methods in biomechanics and biomedical engineering, 2013(ahead-of-print): p. 1-9.
53. Feldmann, D. and C. Wagner, *Numerical simulation of the oscillatory ventilation in simplified human lung models*, in *New Results in Numerical and Experimental Fluid Mechanics VIII*. 2013, Springer. p. 591-598.
54. Yin, Y., et al., *A multiscale MDCT image-based breathing lung model with time-varying regional ventilation*. Journal of computational physics, 2013. **244**: p. 168-192.
55. Sreenivas, K., et al., *Development of an unstructured parallel flow solver for arbitrary Mach numbers*. AIAA Paper, 2005. **325**.
56. Hyams, D.G., et al., *Computational simulation of model and full scale Class 8 trucks with drag reduction devices*. Computers & Fluids, 2011. **41**(1): p. 27-40.
57. Pankajakshan, R., B.J. Mitchell, and L.K. Taylor, *Simulation of unsteady two-phase flows using a parallel Eulerian-Lagrangian approach*. Computers & Fluids, 2011. **41**(1): p. 20-26.
58. ELCAP Public Lung Image Database [cited 2012; Available from: <https://eddie.via.cornell.edu/lungdb.html>].

59. Lorensen, W.E. and H.E. Cline. *Marching cubes: A high resolution 3D surface construction algorithm*. in *ACM Siggraph Computer Graphics*. 1987. ACM.

VITA

Ross Gruetzemacher was born in Hattiesburg, Mississippi, on September 3rd, 1983. In 2001 he attained the rank of Eagle Scout with the Boy Scouts of America and graduated from Gordon Lee High School in Chickamauga, Georgia. In 2011, he graduated from the University of Tennessee at Chattanooga with a Bachelor of Science in Mechanical Engineering. In December 2014, Ross was awarded the Master of Science: Engineering from the University of Tennessee at Chattanooga.